Interactions between buried mass-transport complexes and subsequent slope failures on a passive margin

Nan Wu[1*], Christopher A.-L. Jackson[2], David M. Hodgson[3], Harya D. Nugraha[4,5], Guangfa Zhong[1]

[1]State Key Laboratory of Marine Geology, Tongji University, 1239 Siping Road, Shanghai, 200092, China
[2]Department of Earth Science and Engineering, Imperial College, Prince Consort Road, London, SW7 2BP, UK
[3]School of Earth and Environment, University of Leeds, Leeds, LS2 9JT, UK
[4]Center for Sustainable Geoscience, Universitas Pertamina, Jakarta, 12220, Indonesia
[5]Department of Earth Science, University of Bergen, Allégaten 41, N-5007 Bergen, Norway
*nanwu@tongji.edu.cn

Abstract

Mass-transport complexes (MTCs) are common features on all continental margins, with stacked MTCs indicating repeated slope failure. This suggests MTC generation and emplacement may pre-condition a slope to fail again, although direct evidence for this is currently lacking. Determining the relationship between MTC development and slope stability is important, given its implications for understanding long-term basin evolution and geohazard assessment. Here, we use 3D seismic reflection data from the Kangaroo Syncline, offshore NW Australia, to investigate how pre-existing MTCs can prime subsequent failure events. We interpreted 11 MTCs that constitute approximately 80% of the total stratigraphic of the post-Miocene interval, with individual MTC spanning areas of up to 2500 km². We show that: i) lithological heterogeneity present within a sedimentary succession due to MTC emplacement can impact the location of subsequent slope failures; ii) topography formed by a buried MTC can enhance the erosive ability and effect the transport pathway of subsequent slope failure events; iii) differential compaction between debrite matrix and blocks can produce a rugose MTC top surface that can influence the distribution and stratigraphy of subsequent slope failures; iv) the thickness pattern of buried MTCs can provide a mechanism for predicting the depocentre of future slope failure events; and v) the nature of the sedimentary succession, the aseismic setting, the presence of fluid venting systems, and slope oversteepening can collectively contribute to the preconditioning of recurrent MTCs in the Kangaroo Syncline. Our results show that buried MTCs have profound effects on the location, nature, geometry, and hazard potential of future slope failures. Therefore, investigating the interaction between stacked MTCs is a crucial component of future geohazard impact assessments.

Keywords: Mass-transport complexes (MTCs), Exmouth Plateau, Geohazard assessment, Subaqueous slope failure, Subaqueous landsliding

1. Introduction

The term 'mass-transport complex' (MTC) is applied to a range of gravity-driven, subaqueous deposits resulting from creep, slide, slump, and debris flow processes (e.g. Dott Jr, 1963; Nardin et al., 1979; Nemec, 1990; Posamentier and Martinsen, 2011). MTCs can be very large (>10,000 km^3), and can travel quickly (>50 km/h) over long distances (i.e., >100 km), transporting large volumes of sediment, carbon, and nutrients from continental margins to the deep ocean (e.g., Talling et al., 2014; Kioka et al., 2019). The passage of an MTC can pose a great risk to submarine infrastructures (i.e. hydrocarbon- and windfarm-related platforms, and seabed cables), and generate powerful tsunamis that impact submarine ecosystems and threaten coastal populations (Harbitz et al., 2014; Talling et al., 2014; Lintern et al., 2019; Watkinson and Hall, 2019). The volumetrically largest MTCs on the planet have occurred on passive margins (Masson et al., 2006; Moscardelli and Wood, 2016). However, these giant MTCs are hard to predict, as they are primed and triggered by interacting factors including sea level fluctuations, climate change, substrate character and heterogeneity, sediment supply rates, and tectonic activity (Masson et al., 2010).

On some passive margins, slope failures are frequent, leading MTCs to be the most volumetrically dominant component of basin-fills, where 50%-90% of a succession comprises stacked MTCs (Appendix 1; Solheim et al., 2005; Sawyer et al., 2009; Li et al., 2015; Reis et al., 2016; Nugraha et al., 2018; Omeru and Cartwright, 2019; Steventon et al., 2019; Barrett et al., 2021). The morphology, distribution, kinematics, and priming and trigger mechanisms of some volumetrically significant MTCs, emplaced during a single event, have been considered, such as the Storegga Slide (i.e. Kvalstad et al., 2005), the Baiyun Slide (i.e. Sun et al., 2018), the Gorgon Slide (i.e. Nugraha et al., 2022), and the Amapá Megaslide Complex and Pará-Maranhão Megaslide Complex (i.e. Reis et al., 2016). However, few studies have investigated how pre-existing MTCs influence subsequent slope failures in successions containing stacked MTCs, and even fewer have examined why slope failures in these sedimentary basins can recur repeatedly over long geological timescales (Masson et al., 2006). Here, we investigate the interactions between eleven, post-late Miocene MTCs imaged in high-resolution 3D seismic reflection volume from the Kangaroo Syncline, offshore NW Australia. We seek to answer the following key questions: (i) why are MTCs abundant in the Kangaroo Syncline?; and (ii) what role do pre-existing MTCs play in preconditioning the location, thickness, and volume of material removed, transported, and deposited during future slope failures?

2. Geological setting

The Kangaroo Syncline (or Trough) is a sub-basin of the North Carnarvon Basin, located on the NW Australian continental margin (Figure 1A; Hengesh et al., 2013; Scarselli et al., 2013a). As its name suggests, the Kangaroo Syncline is a c. 100 km-wide, NNE-trending, synclinal depocenter that is defined by a relatively low (0.08°-1.5°) seabed gradient (Hengesh et al., 2013). It is several hundred kilometres long and tens of kilometres wide, with present water depths of 1000-1300 m (Figure 1A; Exon et al., 1992; Hengesh et al., 2013). The Kangaroo Syncline formed in response to several rifting events that most recently occurred between the

Late Jurassic and Early Cretaceous (Longley et al., 2002). During the Late Cretaceous, uplift of the Australian continental hinterland and structural inversion offshore on the southern Exmouth Plateau led to the formation of the Kangaroo Syncline and Exmouth Plateau Arch (Tindale et al., 1998). During the Late Oligocene, the Kangaroo Syncline and the Exmouth Plateau Arch were reactivated due to the collision of the Australian and Eurasian plates (Barber, 1988; Keep et al., 1998; Cathro and Karner, 2006). Following that, in the late Miocene, the collision of the Australian Plate with the Eurasia and Pacific plates led to further growth and deepening, respectively, of the Exmouth Plateau Arch and Kangaroo Syncline (Tindale et al., 1998). From the late Miocene to the Present, continuous collision of the Australian Plate with the Eurasia Plate accelerated tectonic subsidence of the Kangaroo Syncline and inverted rift-related faults beneath the present continental shelf (Hull and Griffiths, 2002).

This study focuses on the late passive margin megasequence (late Miocene to Present). Water depths at this time were bathyal (800-1500 m), with deposition dominated by eupelagic carbonate (Exon et al., 1992; Haq et al., 1992). The study interval lies between Horizon 0 (H0, approximately late Miocene) and the seabed (Figures 1B, 1C). Ocean Drilling Program (ODP) site 762 lies c. 270 km east of the study area (Figure 1A), near the apex of the Exmouth Plateau Arch. Core and geotechnical data from ODP site 762 indicate that the study interval is dominated by highly compressible, low-velocity, water- and foraminifera-rich, carbonate oozes (Figure 1B; Haq et al., 1992; Wu et al., 2023).

3. Dataset and methods

The primary dataset used in this study is the Willem 3D seismic reflection survey, acquired in 2011 (Figure 1A), which covers an c. 2628 km^2 area of the lower continental slope and adjacent depocentre (i.e. the Kangaroo Syncline), in water depths of 200-1500 m (Figure 1A). The 3D seismic reflection data were post-stack time-migrated (PSTM) and are displayed using SEG reverse polarity, where a downward increase and decrease in acoustic impedance are expressed as blue/black (negative) and red/white (positive) reflection events, respectively. The vertical sampling rate of the seismic reflection data is 2 ms, and the bin size of the seismic survey is 25 x 25 m. From the seabed to the study interval, the dominant frequency of the 3D seismic reflection data decreases from ca. 60 Hz to ca. 40 Hz, and the average seismic velocity increases from 1750 m/s to 2000 m/s; we therefore estimate an approximate vertical resolution of 7.3 m at the seabed, decreasing to 12.5 m near the base of the studied interval. The excellent spatial resolution of the 3D seismic reflection data allows a detailed interpretation and characterization of the MTCs' geometries, internal characteristics and emplacement directions.

The interval of interest (late Miocene – Recent; Figures 1B, 1C) correlates to seismic unit 3 of Nugraha et al. (2018) and seismic unit 2 of Wu et al. (2023), who studied the seismic-stratigraphy of adjacent areas. Previous studies indicate that the interval of interest contains MTCs that either originated from the bathymetric highs of the lower NW Australian continental slope, or the upper slope of the Exmouth Plateau Arch (Hengesh et al., 2012; Scarselli et al., 2013a; Nugraha et al., 2018). Twenty-three seismic horizons (H0 to the seabed) have been interpreted to define the base and top of each MTC, based on vertical and lateral changes in seismic facies, the packages they define, and the expression of their bounding surfaces (Figures 2A, 2B). Variance and amplitude contrast attributes, as well as spectral decomposition (RGB blending), have been extracted from the basal shear surface and the top surface of MTCs to identify kinematic indicators that may reveal the MTC emplacement direction and emplacement-related deformation. The variance attribute calculates the variability of a trace to its neighbour over a particular sample interval and produces interpretable lateral changes in acoustic impedance (Van Bemmel and Pepper, 2000). The amplitude contrast attribute calculates the spatial gradient on an image; it improves the edge detection spatially and thereby helps the identification of the terminations of the discontinuities (Aqrawi and Bø, 2016).

Spectral decomposition is a frequency-based seismic attribute that separates the seismic signal into three frequency bands, including red (low frequency), green (mid frequency), and blue (high frequency). When blended, this RGB visualization can help image structural and stratigraphic features within MTCs (Partyka et al., 1999). Isochron (i.e. time-thickness) maps of each MTC are computed from their basal and upper surfaces, with these being used to assess the spatial relationships between subsequent MTCs. Finally, we calculate the dip, width and incision depth of grooves, formed by the dragging of rigid blocks contained at the base of slope failures to quantify the flow direction and the erosional capacity of the MTCs during their emplacement (Bull et al., 2009; Sobiesiak et al., 2018).

4. Results

This study focuses on eleven stacked MTCs (MTC 1-11) that comprise nearly 80% of the stratigraphic thickness of the studied stratigraphic interval (Figures 2A, 2B). The eleven studied MTCs are characterised by packages of chaotic, variable-amplitude reflections (cf. Bull et al., 2009; Posamentier and Martinsen, 2011). They are bound below by a positive polarity, high-amplitude, continuous basal shear surfaces, and above by a medium-amplitude, negative polarity, rugose top surface. In the following section we describe the distribution, external and internal geometry, emplacement direction and kinematics of the 11 MTCs, from oldest (MTC-1) to youngest (MTC-11).

4.1 MTC-1

Description: MTC-1 is internally seismically chaotic and defined at its base and top by H1 and H2, respectively (Figures 2A, 2B). A variance attribute calculated within H1 indicates a tongue-shaped geometry, narrowing to the NNE (Figures 3A, 3B). The western boundary of MTC-1 is defined by an NE-trending erosional margin associated with a younger MTC (MTC-2), whereas its eastern boundary trends N-S and is defined by an erosion surface defining the base of another younger MTC (MTC-4) (Figures 3A, 3B). Below the middle of MTC-1, NNW-trending lateral ramps and E-trending internal ramps are present, with numerous NNE-trending, diverging lineations observable beyond the internal ramp (Figure 3B). MTC-1 is overlain by approximately 300 m of slope deposits and is eroded by later MTC-2 in its western part (Figure 3C). MTC-1 thins to the northeast, and its basal shear surface dips north-northeastwards (Figure 3D).

Interpretation: The geometry of MTC-1 is at least partly an erosional remnant of its primary distribution, due to the later incision by MTC-2 (i.e. in the west) and MTC-4 (i.e. in the east) (Figure 3B); it is thus likely that MTC-1 initially extended further westwards and eastwards. The seismic expression of the predominantly chaotic reflections is typical of an internally highly deformed debrite, similar to other drilled examples of MTCs (Piper et al., 1997). The lineations developed beyond the internal ramp are interpreted as basal grooves (i.e. Posamentier and Martinsen, 2011; Sobiesiak et al., 2018), formed by clasts carried within the host flows that scoured the contemporaneous seabed. Grooves typically form parallel to the MTC transport direction, which together with the NNE downward trending of the basal shear surface, suggest MTC-1 was emplaced towards the NNE (Gee et al., 2005; Bull et al., 2009). Internal and lateral ramps result from MTCs cutting up through stratigraphic levels, creating a step-like geometry in cross-section (Frey-Martínez et al., 2006; Bull et al., 2009). The lateral and internal ramps are considered to trend parallel and perpendicular to the MTCs' transport direction, respectively (Bull et al., 2009). We therefore interpret a NNE translation direction for MTC-1, consistent with that inferred from the grooves (Figure 3B).

4.2 MTC-2

Description: MTC-2 is defined at its base by H3 and its top by H4 (Figures 2A, 2B). A variance attribute calculated within H3 indicates MTC-2 has a semi-elliptic geometry, with its eastern boundary defined by a NE-trending headwall scarp and its western boundary by an erosional ramp associated with the younger MTC-3 (Figures 4A, 4B). The isochron of MTC-2 reveals that it thins westward from its headwall (Figure 4C). The variance attribute indicates that MTC-2 contains numerous parallel to sub-parallel, block-shaped packages in its eastern part (Figures 4A, 4B). In seismic sections, these form ridge-shaped blocks flanked by troughs (Figure 4D). The blocks are 210-300 m high, 170-210 wide, and 800-1,200 m long, with minor internal deformation (Figure 3C, 4D). The intervening troughs are 160-260 m deep, 190-230 m wide, 800-1,200 m long and are defined by a chaotic, variable-amplitude seismic facies (Figure 4D). The lower section of the blocks is characterized by chaotic seismic facies, comparable to those characterising the entirety of MTC-1 (Figure 3C, 4D). The chaotic seismic facies are also bound by medium to high-amplitude, positive reflections, comparable to those bounding MTC-1 (Figure 3C). The blocks decrease in size, lose their block-shaped form, and become internally more deformed westwards (Figure 4D).

Interpretation: MTC-2 was previously described by Wu et al. (2021b), who document a c. 300 m thick succession of undeformed slope strata between MTC-1 and MTC-2 (Figure 4D). Unlike MTC-1, the basal shear surface of MTC-2 lacks kinematic features (i.e. lateral margins, ramps, or grooves; Figure 4A) that record its emplacement direction. Despite this, Wu et al. (2021b) interpret an overall north-northwestward translation direction, along the axis of the Kangaroo Syncline, based on its headwall scarp orientation (i.e., NE-SW) and spatial trends in block size (i.e. blocks decrease in size towards the WNW) (Figure 4B; Wu et al., 2021b). Based on their geometric characteristics and distribution, the intra-MTC blocks are interpreted as being related to lateral spreading (Wu et al., 2021b). The similarity in the seismic facies characterising the intra-MTC blocks and the undeformed strata (i.e. a thin MTC overlain by largely undeformed strata) suggests the former are derived from the latter (Figures 3C, 4D). This is supported by the observations that the blocks in the eastern part of MTC 2 are the same thickness as the laterally adjacent, largely undeformed slope succession (Figures 3C). We therefore interpret that the emplacement of MTC-2 led to erosion of the underlying MTC-1, with portions of MTC-1 being entrained into and forming part of the basal shear zone of MTC-2.

4.3 MTC-3

Description: MTC-3 overlies MTC-2, separated by a thin (c. 30 m) package of slope deposits. It is bounded by H5 and H6 at its base and top, respectively (Figures 2A, 2B). The variance attribute calculated from H5 reveals that MTC-3 has a scallop-shaped geometry in plan-view (Figures 5A, 5B). The eastern boundary of MTC-3 is defined by an NNE-trending scarp, whereas its western boundary is beyond the 3D seismic reflection dataset (Figure 5B). The isochron of MTC-3 shows that it thins eastward, showing an opposing thickness trend to MTC-2 (Figure 5C).

A seismic section through MTC-3 reveals that it comprises blocky seismic facies in the west, chaotic seismic facies near its centre, and semi-continuous, medium-amplitude seismic reflections offset by thrusts faults in the east (Figure 4D). The central region of MTC-3 contains several E to SE trending linear features that are least 7 km long (Figures 5A, 5B). A seismic section shows that the linear features are up to 400 m wide and 60 m deep, and have a U-shaped geometry that truncate underlying reflections (Figure 5D). The eastern region contains numerous broadly eastward-convex, regularly spaced undulations, with the eastern, most distal part of MTC-3, notably coinciding with where the underlying lateral spreads (associated with MTC-2) are developed (Figures 5B, 5E). In detail, the regularly spaced undulations are characterised by semi-continuous, medium-amplitude seismic facies that terminate against the relief created by the underlying lateral spreads (Figure 5E). Further east, the seismic reflections are continuous and drape the lateral spreads, defining low-relief folds (Figure 5E).

Interpretation: The NNE-trending eastern boundary is interpreted as the distal limit of MTC-3, where the deposit changes from principally debritic material to undeformed, slope sediments (Figures 5A, 5B). The linear features at the base of MTC-3 in the west of the seismic survey are interpreted as erosional scours (i.e. Moscardelli et al., 2006), which potentially formed by the sliding or dragging of blocks across the substrate as the MTC was emplaced (Gee et al., 2005; Sobiesiak et al., 2018). The regularly spaced undulations near the eastern boundary of MTC-3 are interpreted as pressure ridges caused by compression or horizontal shortening of transported material, noting that such features are normally convex in the downslope direction (Nissen et al., 1999; Bull et al., 2009). The pressure ridges are underlain by, and likely genetically related to, thrusts, suggesting the failed mass remained frontally confined (Figure 5E; Frey-Martínez et al., 2006). Pressure ridges and scours normally develop perpendicular and parallel to an MTC's main flow direction, respectively (Bull et al., 2009). We therefore interpret that the gross transport direction of MTC-3 was towards the east and south-east (Figure 5B).

The lateral spreads associated with MTC-2 developed considerable positive relief of a few tens of metres overall several kilometres horizontally; we infer frontal buttressing of MTC-3 relief caused shortening and thrusting in its distal part (Figure 5E). MTC-2 and MTC-3 show opposing emplacement directions and thickness trends (Figures 4C, 5C), suggesting that relief associated with the former controlled the bathymetric template onto which the latter was emplaced. After deposition of MTC-3, the paleo-seabed began to heal via the deposition of fine-grained carbonate oozes that drape the top surface of MTC-3 (Figure 5E; Nugraha et al., 2018).

4.4 MTC-4 & MTC-5

Description: MTC-4 is located c. 30 km east of MTC-3, with its base defined by H7 and its top by H8 (Figures 2A, 2B). The variance attribute analysis derived from H7 demonstrates that MTC-4 exhibits a lobate geometry in plan-view (Figure 6A). The eastern and western boundaries of MTC-4 are defined by N and NNW-trending lateral scarps. Spectral decomposition attributes reveal that the distal part of MTC-4 is characterized by fingerprint-like structures, consisting of curved lineations that are convex downslope to the north, offset by NNW-trending longitudinal lineations, oriented perpendicular to the fingerprint-like lineations (Figures 6B, 6C). Seismic section across MTC-4 reveals chaotic, highly discontinuous, medium-amplitude reflections at its updip end (southeastern part), transitioning to isolated, folded, high-amplitude reflections encased within chaotic, transparent reflections near the proximal part. In the downdip part it comprises pairs of high-amplitude, high-angle discontinuities that converge downward onto the basal shear surface (Figure 6D).

MTC-5 overlies MTC-4, separated by c. 30-50 m thick slope deposits, and is bounded by H9 at its base and H10 at its top (Figures 2A, 2B). Variance attribute analysis extracted from H9 reveals that MTC-5 is characterized by NNE-trending updip and distal margins, as well as a NNW-trending northern lateral margin (Figure 7A). Like MTC-4, the proximal and distal parts of MTC-5 exhibit fingerprint-like structures with a convex-downslope geometry, characterized by lineations overall striking NNE–SSW (Figures 7B, 7C). The distal morphology of MTC-5 is characterized by multiple lobate features that exhibit cross-cutting relationships, and which are bounded by NNW-trending, longitudinal margins (Figure 7B). Internal lineations are more intensely deformed close to these margins. Seismic section reveals that the basal shear surface of MTC-5 incises multiple stratigraphic levels and is associated with variable internal seismic facies. For example, in the updip region of MTC-5 is dominated by chaotic reflections, whereas the proximal region is characterised by high-amplitude, high-angle discontinuities that cut upward from the basal shear surface (Figure 7D). The distal region is dominated by thrust-bounded blocks that preserve coherent stratigraphy, whereas the intervening zones exhibit disrupted reflections or acoustically chaotic facies. Further downslope, the basal shear surface steps upward into shallower stratigraphic levels, where it is overlain by steeply dipping, closely spaced faults (Figure 7D).

Interpretation: The N and NNE-trending scarps flanking MTC-4 are interpreted as its lateral margins; their trend suggests the deposit was transported broadly northwards (Bull et al., 2009) (Figure 6C). The continuous lineations that are deformed into curvilinear, fingerprint-like structures in map view, and which correspond to reflection discontinuities in the seismic section, are interpreted as forethrusts and back-thrusts uplift internally coherent pop-up blocks (Nugraha et al., 2020). The high-angle discontinuities are interpreted as contractional thrusts that commonly accommodate a major portion of the total downslope shortening (Frey-Martínez et al., 2006). The longitudinal lineations perpendicular to the strike of the fingerprint-like structures are interpreted as longitudinal shear zones, which form due to velocity contrasts between adjacent flow compartments during MTC emplacement (Steventon et al., 2019; Nugraha et al., 2020; Abu et al., 2022).

The NNE-trending updip and downdip margins of MTC-5 are interpreted as the headwall scarp and distal margin, respectively (Figure 7C), marking the boundary between the deformed region and the surrounding undeformed slope (Bull et al., 2009). Similar to MTC-4, the fingerprint-like structures are interpreted as compression-related features, whereas the cross-cutting lobes are considered to represent discrete flow cells that accommodate across-strike variations in the total magnitude of down-dip transport, bounded by longitudinal shear zones (Steventon et al., 2019; Nugraha et al., 2020). The chaotic reflections are interpreted as debrite, the high-amplitude, high-angle discontinuities as contractional thrusts, and the thrust-bounded blocks as pop-up structures. In both MTC-4 and MTC-5, the along-strike transition from chaotic debrite to well-defined pop-up blocks and thrusts reflects progressive frontal compression during the final stages of emplacement. This structural complexity is influenced by factors such as frontal confinement (buttressed vs. emergent runout), internal flow compartmentalization, and multi-phase deformation, all of which contribute to and record the complex kinematic interactions and strains at the front of an MTC as it stops (Abu et al., 2022).

4.5 MTC-6 & MTC-7

Description: MTC-6 is separated from MTC-5 by an 80–160 m thick package of slope deposits in the eastern part of the study area, and is bounded by H11 at its base and H12 at its top (Figures 2A, 2B). A variance attribute map reveals MTC-6 has a W- to SW-trending southern margin and a N- to NE-trending distal margin (Figures 8A, 8B). The basal shear surface of MTC-6 is locally defined by a broadly NNW-trending continuous scarp that is flanked by two sets of lineations. South of the scarp, the lineations trend NNW whereas to the north they trend a NW. MTC-6 is mainly composed of chaotic seismic facies, underlain by a high-amplitude, positive-polarity basal shear surface (Figure 8E). The basal shear surface extends further upslope, where it serves as the basal boundary for multiple younger MTCs (i.e., MTC-7, MTC-8 and MTC-9; see below).

MTC-7 is deposited directly above MTC-6, being bounded by H13 at its base and H14 at its top (Figure 8E). The variance attribute map extracted through MTC-7 reveals it is bounded by a NNE-trending margin defining its updip extent, and a NNW-trending margin delineating its downdip extent. The southwestern part of MTC-7 is partially incised by the subsequent MTC-8 (Figures 8C, 8D). Internally, MTC-7 contains NNW-trending lineations in its proximal part, a concave-downward, semi-enclosed scarp in its southeastern part, and a NNW-trending scarp in its northeastern part. Seismic sections reveal that this MTC is internally chaotic, with its basal shear surface partially merging with that of the underlying MTC-6 in the shared headwall region (Figure 8E).

Interpretation: The W- to SW-trending southern boundary of MTC-6 is interpreted as the lateral margin of the deposit, whereas the N-trending represents its distal margin (Bull et al., 2009). The NNW-trending basal lineations of MTC-6 are interpreted as grooves. Accordingly, we interpret that the MTC-6 was emplaced toward the NNW, parallel to the dip direction of the grooves. The NNW-trending continuous scarp is interpreted as an internal ramp, where the basal shear surface stepped upward into shallower strata during emplacement, resulting in a shift of groove orientation from NNW-SSE to NW–SE.

The NNE-trending margins that define the updip and downdip extents of MTC-7 are interpreted as the headwall scarp and distal margin, respectively. The NNW-trending lineations are interpreted as basal grooves, whereas the NNW-trending scarp is interpreted as an internal ramp. Based on the orientation of the headwall scarp and basal grooves, we interpret the transport direction of this MTC was towards the NNW. The partially overlapping basal shear surfaces indicate that during its emplacement, MTC-7 eroded into the underlying MTC-6 in the headwall region, causing the basal shear surfaces of the two MTCs to merge. This, in turn, suggests that the basal shear surface of the buried MTC-6 locally influenced the maximum erosion depth of the subsequent slope failure.

4.4 MTC-8

Description: MTC-8 directly overlies MTC-7 in the eastern part of the study area, whereas it is separated from MTC-3 by a 30-70 m thick package of slope deposits in the western part (Figures 2A, 2B). MTC-8 is bounded by H15 at its base and by H16 at its top (Figure 8E). The amplitude contrast attribute extracted from the BSS of MTC-8 (H15) is characterized by a NW-trending lateral margin on its northeastern side and NW-oriented internal ramp structures within its central region (Figures 9A-9C). The isochron of MTC-8 shows it is thinnest in its middle and thickest in its western and eastern portions (Figure 9D). Curvilinear lineations are observed on the basal shear surface beneath both the northeastern and southwestern regions of MTC-8 (Figures 9B, 9C). In the northeastern region, these sub-parallel lineations extend for 30-50 km in a NW-direction. Seismic sections reveal that the lineations are erosional, containing block-shaped packages incised into the BSS and underlying relief capping MTC-7, and delineating a prominent channel-like geometry on the basal shear surface (Figure 10A). These block-shaped packages are 80-220 ms (approximately 60-150 m) in thick and 700-1100 m wide. Internally, they are characterized by highly deformed to transparent reflections, exhibit angular to sub-angular morphologies, and are embedded within a seismically chaotic matrix (Figure 10A). In its central region, the basal shear surface exhibits a finger-like protruding structure, characterized by short, NNE-trending lineations (Figure 10B). These lineations correspond to high-amplitude, discontinuities or folded, and steeply dipping reflections observed in seismic section (Figure 10C). Additionally, this finger-like, protruding structure occurs directly above MTC-7, with the internal steeply dipping reflections terminating against it (Figure 10C).

In the southwestern region, where MTC-8 caps MTC-3, MTC-8 is locally thick where the underlying MTC-3 is thin, and vice versa (Figure 9D). In this region, the lineations are 20-40 km long and show a radial distribution pattern (Figures 9B, 9C, 11A). The lineations are erosional, defining a prominent V-shaped geometry, and are 12-50 ms deep and 50-300 m wide (Figures 9D). The terminations of the lineations exhibit a semi-elliptical morphology, within which the seismic data reveal rounded edges and angular blocks (Figure 11A). In the same area, we observe that the NW-trending internal ramp on the basal shear surface is superimposed above the headwall scarp of the buried MTC-2 (Figures 9D, 11A). The NE-trending internal ramp along the BSS of MTC-8 separates lineations of two different trends (Figures 11A). To the SE of the internal ramp, they trend NW to NNW (315-330°), whereas to the NW of the internal ramp they trend NNE to NE (015-045°), broadly parallel to the axis of the Kangaroo Syncline (Figures 11D). Additionally, the lineations exhibit a V-shaped geometry southeast of the internal ramp, transitioning to U-shaped profiles northwest of it (Figure 12). To assess how erosion varies across the NE-trending internal ramp, we pick one of the most continuous lineations (G-1; Figure 11A) to quantify down-trend variations in its width and depth. From the SE to the NW of the internal ramp, the width and erosion depth of G-1 increases sharply from 110 to 270 m and 18 to 45 ms, respectively (Figure 11E).

Interpretation: The block-shaped features associated with the scours and high relief on the top surface in the northeastern region of MTC-8 are interpreted as megaclasts (Figure 10A). These are large clasts ranging from hundreds of meters to kilometers in diameter, transported within MTCs (Jackson, 2011; Hodgson et al., 2018). The transparent internal reflections and angular to sub-angular morphologies, suggesting they were well-consolidated prior to entrainment (Hodgson et al., 2018). Interaction between these megaclasts and the underlying substrate generated deep erosional scours into the substrate, thereby modifying the morphology of the basal shear surface and deforming MTC-7.

In the central region of MTC-8, the lineations within the finger-like protruding structure are interpreted as fold-and-thrust belts formed during compression towards the toe domain of the MTC (Figures 10B, 10C; Steventon et al., 2019). Given that these features spatially overlap with remnant relief above the underlying MTC-7, we suggest that this relief caused the deceleration of, and compression and shortening within, the subsequent mass flow (e.g., Figure 10C).

The curvilinear lineations developed in the northwestern region are interpreted as grooves (Posamentier and Kolla, 2003; Gee et al., 2005). The observation of clasts within the grooves supports that they were transported at the base of the debris flow and acted as erosional tools during submarine landsliding (Peakall et al., 2020; Figure 11C). Therefore, the variation in orientation, cross-sectional geometry, and scale of grooves across the NE-trending internal ramp suggests flow divergence during the emplacement of MTC-8. The presence of the NE-trending internal ramp corresponds to an area where MTC-8 incised into deeper stratigraphy and thickened as a result (Figures 9E, 11A). The thickness change in MTC-8 across the internal ramp reflects the thickness pattern of MTC-3, where unhealed relief remained near the headwall of MTC-2 (Figure 9E).

The groove trend along the BSS of MTC-8 suggest it was steered away from a shallower area in the SE and cut down to be more confined to the NW (Figures 11A, 12). The grooves are wider and deeper to the NW, suggesting either larger megaclasts are entrained from the ramp, or given the continuity of grooves, that the megaclasts were able to gouge deeper into the substrate (Figure 11). The thickness of MTC-8 thus increases in the area of the MTC-2 and 3 headwall resulting the generation in a downstream-facing ramp (Figures 9A, 9D). Therefore, we suggest that MTC-2 and 3 controlled local seabed topography that influenced the emplacement of MTC-8, enhancing its erosive ability, diverting its flow direction, and providing a focal point for its ultimate deposition.

4.5 MTC-9

Description: MTC-9 directly overlies MTC-8 and is bounded by H17 at its base and by H18 at its top (Figure 8E). The amplitude contrast attribute calculated on H17, the BSS of MTC-9, reveals that the overlying deposit is the most aerially extensive in the study area (at least 2500 km^2; Figures 13A, 13B). The isochron of MTC-9 displays a tripartite thickness distribution, being thickest in the NW and SE portions, and thinner in-between (Figure 13C). MTC-9 is bounded updip by an NE-trending scarp located in the southeastern part of the study area that separates the internally deformed area from the undeformed substrate. Several asymmetrical, sparsely distributed blocks are observed to the NW of this scarp and in the northeastern region (Figures 13A, 13B). The presence of these blocks results in a rugose top surface of MTC-9, exhibiting localized topographic highs (Figure 13D).

Based on their internal deformation intensity and external geometry, three distinct block types are identified: (i) highly deformed blocks, up to 300 m diameter and 180 m thick, that are located in the proximal region and associated with NNW-trending lineations that incise the underlying substrate by several tens of meters and cone-shaped ridges of the underlying deposit (Figures 14A, 14B). These blocks are characterized by chaotic to transparent internal reflections, with angular to sub-angular terminations at their top surface (Figures 14C, 14D). (ii) moderately deformed blocks, up to 2.7 km diameter and nearly 300 m thick, located near the headwall region, and as such, inferred to have remained relatively in-situ during MTC emplacement (Figure 15A). These blocks are characterized by semi-continuous, faulted and folded internal reflections, have rounded to sub-rounded external geometries, and rest on a planar basal surface (Figures 15B, 15C). Seismic reflections overlying these blocks exhibit clear onlap terminations onto the top surface of the MTC-9, with seismic reflections draping against both flanks of the topographic highs (Figure 15B). The lower part of these blocks, corresponding to the basal shear surface, is typically marked by deformed to chaotic seismic reflections (Figure 15C); and (iii) tabular shaped blocks, located near the MTC proximal region. The long axes of these blocks trend NW and are up c. 17 km long (Figures 13A, 13B). These blocks are internally defined by undeformed, continuous reflections that are abruptly bounded by chaotic seismic reflections characterising the main body of MTC-9 (Figure 15D). No visible basal deformation is observed directly beneath the in-situ blocks (Figure 15D).

Interpretation: We interpret the lineations in MTC-9 as emplacement-related scours and the scarp defining its SE margin as a headwall scarp. The location of the headwall scarp defines the source area of the slope failures (Bull et al., 2009; Posamentier and Martinsen, 2011); thus, given the headwall scarp of the MTC-9 is located on the lower continental slope, we infer it was sourced from here and transported northwestward. This interpretation is consistent with the NW-SE trend of the basal scours (Figure 13B). The moderately deformed blocks developed near the headwall scarp are interpreted as transported blocks representing relatively competent pieces of failed material that have been transported within the MTC (Figures 15A, 15B; i.e. Frey Martinez et al., 2005; Bull et al., 2009). The highly deformed blocks developed in the eastern part of MTC-9 are interpreted as megaclasts, representing failed material that were rotated during transport and travelled a relatively long distance (Figures 14C, 14D; Nwoko et al., 2020). The internally undisturbed block is interpreted as a remnant block of substrate surrounded by failed and transported material within the main MTC body (Figure 15D; i.e. Frey Martinez et al., 2005; Bull et al., 2009).

The megaclasts and transported blocks are sufficiently thick to remain unburied by MTC-9, protruding above the top surface and even the modern seabed, as evidenced by the onlap of younger sediments against their flanks (Figures 14C, 14D, 15B, 15C). Given their substantial thickness, the transported blocks and megaclasts likely originated from the headwall region and are interpreted to have been entrained and carried downslope within the debris flow during transport. Localized uplifted topography, exceeding 120 m in relief, formed a series of seamount-like structures on the paleo-seabed, which continue to influence modern seabed morphology (Figures 14D, 15B, and 15C). These features act as barriers to subsequent MTC-10 and MTC-11.

4.5 MTC-10 & MTC-11

Description: MTC-10 directly overlies MTC-9, with its base and top defined by H19 and H20, respectively (Figure 14C). MTC-10 broadly trends NW, is confined to the NE part of the study area, and has a tabular geometry in plain view (Figures 16A). The eastern and western boundaries of MTC-10 are characterized by NW-trending margins (Figure 16A). The isochron of MTC-10 reveals it is thick in areas where the underlying MTC-9 is thin, and thin or absent where the underlying MTC-9 is thick (Figures 13C, 16B). The seismic section of MTC-10 consists of a package of chaotic seismic facies that thins and pinches out toward the local topographic high associated with positive relief along the upper surface of MTC-9 (Figure 17A).

MTC-11, overlies MTC-10, with its base and top defined by H21 and seabed, respectively (Figure 17A). Like MTC-10, MTC-11 trends NW and is confined to the northeastern part of the study area (Figures 16C, 16D). It exhibits a tongue-shaped geometry characterized by two distinct lobate forms in the northwest. The eastern and western boundaries of MTC-11 are defined by NW-trending margins that parallel to those of the underlying MTC-10 (Figures 16C, 16D). The isochron map of MTC-11 indicates that it is thick in areas where the underlying MTC-9 is thin, and conversely, thin or absent where MTC-9 is thick (Figure 16D). In a similar manner to MTC-10, MTC-11 is internally chaotic and thins and pinches out toward the local topographic high associated with positive relief along the upper surface of the underlying MTC-9 (Figures 16E). MTC-11 is obstructed and frontally confined by topographic barriers formed by pre-existing blocks within the underlying MTC-9, resulting in a relatively short run-out distance of approximately 23–30 km (Figure 17B). In contrast, where the underlying blocks are absent, MTC-11 overrides the existing seabed topography extends downslope beyond the limits of the 3D seismic dataset (Figure 17C).

Interpretation: The NW-trending margins associated with MTC-10 and MTC-11 are interpreted as their lateral margins (Figure 16A). Based on the trend of these lateral margins, we interpret that MTC-10 and MTC-11 were emplaced towards the NW. The depocenters of MTC-10 and MTC-11 overlap spatially above the thinner sections of the underlying MTC-9, suggesting that the seafloor relief created by MTC-9 influenced the deposition of the former two deposits (Figure 16E). The central part of MTC-11 is classified as frontally confined, given it is characterised by an abrupt frontal termination (Frey-Martínez et al., 2006). This confinement results from pre-existing topographic barriers formed by blocks within the underlying MTC-9, which impeded further downslope translation. In contrast, the lobate regions of MTC-11 represent frontally emergent domains, where the MTC seemingly overrode subtle seabed relief and propagated freely downslope, resulting in a longer runout distance. These contrasting frontal styles highlight the complex and spatially heterogeneous emplacement dynamics of MTC-11 (Nugraha et al., 2020).

5. Discussion

We show that the post-Miocene succession of the Kangaroo Syncline is dominated by stacked MTCs. In this section we consider the potential controls on the relative abundance of MTCs in the Kangaroo Syncline, discuss how earlier MTCs can influence the location and scale of subsequent slope failures, and consider the implication of our results for predicting the future occurrence of MTCs and related geohazards and mitigating their impacts.

5.1 Why was MTC emplacement common in the Kangaroo Syncline during the Neogene?

The interplay of factors controlling recurrent submarine landslides along tectonically stable passive margins remain poorly understood. In the Kangaroo Syncline, the stacked MTCs indicates it has been a major depocenter for material originating from adjacent slope failures, which potential pose geohazard risks to existing and planned subaqueous infrastructure offshore NW Australia (Piper et al., 1999; Hengesh et al., 2012; Gavey et al., 2017; Pope et al., 2017). Therefore, investigating the controlling factors for recurrent slope failure within the Kangaroo Syncline could provide insights that are more broadly applicable to other MTC-rich sedimentary systems on passive margins worldwide.

5.1.1 Sediment Properties and their Role in Slope Failure

In the Kangaroo Syncline, carbonate ooze, which consisting of fragile foraminifera and nannofossils, has been the dominant sediment deposit since the late Miocene (Nugraha et al., 2018). Carbonate oozes are highly compressible and have distinct geotechnical characteristics, including high water content (i.e. >50%), low permeability, and low shear strength compared to fine-grained siliciclastic sediments (von Rad, 1992; Urlaub et al., 2015; Gatter et al., 2021). The continuous deposition of carbonate oozes can result in sudden dewatering that causes an increase in sediment pore pressure, resulting in a sufficient excess pore pressure to precondition a low-gradient slope to fail (e.g. Tanaka and Locat, 1999; Volpi et al., 2003; Davies and Clark, 2006). Furthermore, the amount of water stored within shell chambers and skeletal pores in ooze can be as high as 15% of their dry weight (Palmer-Julson and Rack, 1992; Rack et al., 1993). The crushing of fragile biogenic particles could lead to further expulsion of intraparticle water (Urlaub et al., 2015). Laboratory experiments suggest that carbonate oozes are more susceptible to failure than siliciclastic sediments (Gaudin and White, 2009). During the shear strength cyclic T-bar test of carbonate oozes and siliciclastic sediments, the residual shear strength of carbonate oozes drops rapidly to only 10% of their initial strength, whereas the residual strength of siliciclastic sediments can be up to 55% of their initial strength (Figure 18A; Gaudin and White, 2009). Consequently, carbonate oozes lose shear strength rapidly when their strain-bearing capacity is exceeded. This property may explain why slope failures occur frequently in carbonate ooze-rich settings, even on very gently dipping slopes characterised by low rates of sediment accumulation, such as the Kangaroo Syncline. However, the exact failure mechanisms require investigation through drilling derived physical properties before and after failure.

The northwest Norwegian continental margin exhibits similar sedimentological and geotechnical properties, with slope failure and the emplacement of large MTCs repeatedly occurring during the Quaternary, at intervals of approximately 100,000 years (Bryn et al., 2005; Solheim et al., 2005). Sediments in this region, particularly fine-grained biogenic marine oozes interbedded with glaciogenic deposits, are characterized by exceptionally high water content (70% to 90%; Lawrence and Cartwright, 2010; Bellwald et al., 2024). The result is sediments with extremely low bulk densities and high compressibility (Bellwald et al., 2024). Such sedimentological properties enhance pore-pressure accumulation and markedly reduce sediment shear strength, providing ideal conditions for slope instability (Kvalstad et al., 2005). Consequently, these fine-grained, high-water-content sediments inherently predispose slopes along the Norwegian margin to recurrent, large-scale submarine slope failures, in a similar way to the Kangaroo Syncline.

5.1.2 Fluid Venting System and Vertical Fluid Migration

Excess pressures generated by fluid and/or gas migration may precondition a slope to fail (Bünz et al., 2005; Berndt et al., 2012), with this also being true for the Kangaroo Syncline (Wu et al., 2023). In the latter case, excess pore pressure had, and possibly still has, two sources. First, silica diageneses (opal-A to opal-CT conversion) during the burial of the Eocene, chalk-rich succession, which led to fluid expulsion and overpressure development (Wu et al., 2023). A similar mechanism is proposed for a submarine landslide in the Faroe-Shetland Channel, NW offshore UK (Davies and Clark, 2006). Second, gas was likely migrating from the hydrocarbon-bearing Mungaroo Formation (Triassic) during the Neogene, again leading to overpressure development in the shallower stratigraphy (Paganoni et al., 2019; Velayatham et al., 2019). A similar priming mechanism has been identified offshore Norway, in this case in association with gas hydrate dissociation and migration from beneath the main headwall of the Storegga Slide (Sultan et al., 2003; Strout and Tjelta, 2005). Similar fluid migration processes have also been proposed as key preconditioning factors for slope instability in other regions, including the Baiyun Slide complexes in the South China Sea (Li et al., 2014) and the stacked

MTCs in the Taranaki Basin, offshore New Zealand (Ilg et al., 2012). Therefore, sedimentary basins characterised by widespread, sustained, and more importantly, focused gas or fluid generation and migration pose higher risk of slope failure, such as in Kangaroo Syncline.

5.1.3 The Relationship Between Seismicity and Sediment Properties

Although the collision between the Australian and Eurasian plates has generated seismicity since the late Miocene, the Exmouth Plateau is considered a relatively stable, low seismicity passive margin setting (Albini et al., 2013; Nugraha et al., 2018). The seismicity of an area can alter the initial (i.e., immediately post-depositional) sediment properties. For example, siliciclastic sediments within the first 100 m below the seabed that are exposed to repetitive low-magnitude earthquakes can progressively increase their shear strength through shear-induced compaction and dewatering (a process termed seismic strengthening; Sawyer and DeVore, 2015; Ten Brink et al., 2016). Therefore, siliciclastic sediments on active margins typically have higher undrained shear strength and can withstand higher static and dynamic shear stresses than sediments at equivalent depths on relatively aseismic passive margins (Figure 18B; Nelson et al., 2011; Sawyer and DeVore, 2015; Ten Brink et al., 2016). Conversely, when repetitive seismicity (thus the seismic strengthening process) is absent, sediments have lower shear strengths (Figure 18B) and are more susceptible to slope failures than those on active margins (i.e. Sawyer and DeVore, 2015; DeVore and Sawyer, 2016). The shear strength of the carbonate ooze in the Kangaroo Syncline ranges from 1.2 kPa to 12.5 kPa in shallow (i.e., <100 meters below seabed) sediments (Figure 18B), which is at the lower end of the passive margin trend and does not show any evidence for seismic strengthening (i.e., the undrained shear strength is markedly lower than values characterising active margins). Carbonate oozes in Kangaroo Syncline may thus be extremely unstable due to their extremely low shear strength that in part is linked to the low seismicity of the margin.

5.1.4 Slope Steepening Driven by Tectonic Uplift and Sedimentation

During the mid to late Miocene, the northward collision of the Australian Plate with Eurasian microplates induced compressional deformation offshore NW Australia, resulting in broad folding of the seabed and the formation of the Exmouth Plateau Arch (Boyd et al., 1993). This tectonic uplift increased the seabed gradient between the plateau arch and the adjacent continental slope (Figure 1C). Since the late Miocene, the region has experienced widespread MTC emplacement, with sediment sourced from the uplifted plateau arch and adjacent slope (Hengesh et al., 2013; Scarselli et al., 2013b). Published studies attribute the development of widespread MTCs sourced from the uplifted plateau arch and adjacent slope to tectonically induced tilting and folding of the seabed, which enhanced slope gradients and promoted gravity-driven sediment failures (Nugraha et al., 2018).

Similar features have been observed in the Qiongdongnan (QDN) Basin, northern South China Sea, where recurrent slope failures have occurred since the late Miocene, leading to the accumulation of stacked MTCs. During the late Miocene, tectonic uplift of the Himalaya–Tibetan Plateau intensified erosion and weathering in its catchment areas, substantially increasing the sediment supply transported by the paleo-Red River into the QDN Basin (Zhao et al., 2019; Li et al., 2022). In response to this increased sediment flux, the continental margin began to prograde, constructing large-scale clinothems with steep foresets that advanced basinward (Chen et al., 2020). These stacked clinothems led to slope oversteepening and widespread instability, culminating in the development of extensive MTCs throughout the Pliocene succession. A comparable process has been documented in the Taranaki Basin (New Zealand), where tectonic uplift enhanced sedimentation rates and drove the formation of extensive clinoform systems, steepening the paleo-seafloor gradient and preconditioning the margin for repeated slope failure (Sharman et al., 2015; Franzel and Back, 2019).

In summary, the high abundance of MTCs in the Kangaroo Syncline reflects the combined influence of persistent carbonate ooze deposition, excess pore pressure associated with vertical fluid migration, tectonically induced slope steepening during the mid to late Miocene, and extremely low sediment shear strength due to the absence of seismic strengthening.

5.2 How do pre-existing MTCs influence later slope failures?

We identify five ways that pre-existing MTCs can influence the emplacement of subsequent slope failures.

5.2.1. Buried MTCs and their Role in Slope Failure Preconditioning

An overriding MTC can drive density increases and permeability decreases in the substrate, resulting in shear compaction (Wu et al., 2021a). The basal shear surfaces of MTCs are generally more consolidated than lithologically comparable slope or basin-floor strata, showing high bulk density and shear strength, low porosity and permeability. Basal shear surfaces may therefore represent intra-stratal hydraulic boundaries, influencing or limiting fluid migration and the related distribution of overpressure, and thus the overall strength profile of the sedimentary succession (Wu et al., 2021a).

In the Kangaroo Syncline, prior to the emplacement of MTC-2, the basal shear surface of MTC-1 may have formed a hydraulic boundary within the carbonate ooze-dominated succession (Figure 3C). This hydraulic boundary may have permitted the build-up of excess pore pressure and generation of weak layers within the substrate, ultimately priming slope failure and the formation and emplacement of MTC-2.

5.2.2. Relief-Induced Partitioning as a Kinematic Control on Subsequent Slope Failures

MTC emplacement can remould the seascape, creating giant, scarp-bound seabed depressions that cover thousands of square kilometres, and that change the slope profile, potentially making future failures more likely (i.e. Kneller et al., 2016). Previous studies suggest that relief above MTCs influence pathways of subsequent sediment gravity flows. However, the way in which pre-existing MTCs control the flow direction, depositional pattern, and stratigraphic architecture of subsequent failures has received less attention.

In the Kangaroo Syncline, we show that the large blocks (c. 300 m thick) within MTC-2 formed substantial relief (i.e., >100 m and that extends 10's of km laterally) on the contemporaneous seabed (Figure 4D). This relief controlled the down-dip extent and style of strain within MTC-3, with shortening and thrusting occurring where it impinges on this relief (bathymetrical control; Figures 5E). Whereas MTC-3 largely healed the accommodation created by failure of slope material comprising MTC-2, some accommodation remained between blocks within MTC-2. For example, the remaining accommodation above MTC-3 contributed to the partitioning of MTC-8 (Figure 9A, 9D). Slope breaks formed by relief along MTC-2 are expressed within the basal shear surface of MTC-8, evident as the relief of MTC-8's basal shear surface is lower immediately adjacent to the headwall scarp of MTC-2, accompanied by directional changes in striation patterns and thus emplacement direction, and increases in both the incision depth and width of basal grooves (Figures 11A-C). This indicates the former controlled the emplacement direction and erosional capacity of the latter. Relief associated with pre-existing MTCs can therefore serve as structural weak zones (i.e., deformational foci) that localize deformation, influence the emplacement, distribution, and erosional capacity of subsequent MTCs. This is consistent with the findings of Safadi et al. (2017), who demonstrate that large-scale buried MTCs can form a seabed low, acting as long-lived deformational foci that influence the subsequent MTCs over a few hundred thousands of years. Since the main energy of the tsunami waves travel in the direction of slope failure motion, the failure direction is as important as the speed and scale of movement (Driscoll et al., 2000; Schnyder et al., 2016). We suggest that conducting subsurface and surface mapping of MTC top surfaces, particularly at locations where large blocks and scarps exist, could help in predict future slope failure routes and potential danger zones (i.e., pathways for subsequent failure processes), thereby reducing geohazard risks to seabed infrastructure.

5.2.3. Basal Shear Surfaces as Erosional Limits to Recurrent Slope Failures

Commonly, the basal shear surface of MTCs is expressed as a high-amplitude, continuous seismic reflection with reversed polarity relative to the seabed, representing the densest part of the deposit. Such surfaces may also serve as a key kinematic boundary, along which slope failure occurs and MTCs are translated (Shipp, 2004; Sawyer, 2007; Wu et al., 2021a). In the Kangaroo Syncline, MTC-6 has an extensive basal shear surface with a minimum mapped area of ~1,800 km^2 (Figures 8A, 8B). Subsequent MTCs (MTC-7 to MTC-9) share this basal shear surface near the headwall region, indicating a composite kinematic boundary for recurrent slope failure (Figure 8E). The shared basal shear surface of the stacked MTCs in the Kangaroo Syncline suggests that the basal shear surface of the buried MTCs, particularly MTC-6, acted as a structural detachment for subsequent mass-transport events. Although later MTCs may erode or deform the underlying deposits, the initial basal shear surface likely represents a mechanically strong and compacted boundary that resists further incision. This mechanical boundary may limit the depth of subsequent failure surface propagation, thereby constraining the volume of sediment that can be entrained and transported during subsequent slope failures.

5.2.4. Long-Term Seabed Shaping by Differential Compaction Over Buried MTCs

Differential compaction is intrinsic to MTC emplacement, driven by rheological contrasts between rapidly compacting ductile debris flows and less-deformed transport or remnant blocks (Alves, 2010). This results in downward bending of strata over debritic material and upward bending over blocks, producing rugose MTC top surfaces with notable relief (e.g., Alves and Cartwright, 2010). Such compaction can persist for millions of years, shaping seabed morphology and influencing slope depositional patterns (e.g., Alves, 2010; Ward et al., 2018).

In the Kangaroo Syncline, differential compaction between megaclasts or transported blocks and the surrounding debritic matrix has produced significant topographic relief, ranging from tens to over a hundred meters in height and hundreds of meters in width (Figures 14C, 14D, 15B, 15C). These protruding megaclasts, termed "shield blocks" (Rusconi, 2017), can act as physical barriers that obstruct, deflect, or modify the dynamics of succeeding slope failures. For example, the top surface of MTC-9 preserves distinct bathymetric highs, indicating that these irregularities remained exposed and were not buried during the deposition of MTC-9 (Figures 15B, 15C). When subsequent slope failures encounter these obstacles, the flow is forced to diverge around them, potentially generating localised downslope turbulence with enhanced erosive capacity against the substrate. This is evidenced by the basal shear surface (BSS) of the subsequent MTC, which exhibits a steep gradient and increased thickness on the lee side, and a reduced thickness on the gentle stoss side above the buried blocks, indicating that debris flows had enhanced erosive capacity in these zones (e.g., Figure 15B). This turbulence persists some distance, until the younger MTC is physically impeded by the underlying blocks. This mechanism is analogous to the transition from a normal to a supercritical turbidity current, in which flow rheology is highly influenced by pre-existing bathymetric highs (e.g., Covault et al., 2017; Fildani et al., 2021).

In the case of MTC-11, the deposit exhibits a hybrid frontal morphology, i.e., it is frontally confined in its central portion, where blocks within the underlying MTC-9 act as topographic barriers, whereas its lobate margins are frontally emergent, reflecting the absence of such obstacles (Figures 16C, 16D). This spatial variability underscores the critical role of inherited relief, generated by differential compaction, in modulating the rheology of the overriding flow and potentially enhancing the run-out distance of the subsequent MTC (e.g., Moernaut and De

Batist, 2011; Nugraha et al., 2020). Therefore, block-induced differential compaction within buried MTCs can generate basal topographic obstacles that exert a first-order control on the frontal style and kinematic behaviour of ensuing mass movements, ultimately influencing their downslope translation and run-out distance.

5.2.5. Mapping Buried MTCs to Predict Future Slope Failure Depocenters

Slope failure is often associated with the formation of large evacuation zones and steep headwall scarps (e.g., Solheim et al., 2005; Nugraha et al., 2022). In the Kangaroo Syncline, the initiation of MTC-2 created a large evacuation zone characterised by >200 m of vertical relief and a c. 30 km long, NNE-SSW oriented headwall scarp (Figure 4A). This headwall scarp separated the paleo-seabed into bathymetrically high and low areas in the east and west, respectively. This feature subsequently influenced the relief associated with the basal shear surface of younger MTCs. For example, the basal shear surfaces of subsequent MTC-8 and MTC-9 dip relatively steeply near MTC-2’s headwall scarp (Figures 9A, 13A). The headwall scarp associated with MTC-2 also influenced the thickness distribution of subsequent MTCs. For example, MTC-8 is thicker in the low area immediately adjacent to the headwall scarp of MTC-2 (Figure 13). The headwall scarp of pre-existing MTC-2 may therefore control seabed relief and local thickness changes in younger MTCs for a relatively long time after initial formation.

In the Kangaroo Syncline, the spatial distribution of younger MTCs is often controlled by local topographic highs generated above pre-existing MTCs, with their boundaries coinciding with areas where pre-existing MTCs are locally thickest (i.e., MTC-2 vs MTC-3; MTC-9 vs MTC-10; Figure 17). We show that in areas where pre-existing MTCs are relatively thick, subsequent MTCs are relatively thin, and vice versa. For example, the deposition of MTC-9 exhibits a thick-thin-thick pattern (Figure 13C), and the younger MTC-10 is confined to areas where the underlying MTC-9 is relatively thin (Figure 16B); a similar thickness inter-relationship occurs in younger stratigraphy, with MTC-11 being restricted to areas where the underlying MTC-9 is relatively thin (Figure 16D). We note the emplacement of a younger MTC may erode pre-existing MTCs, modifying their original thickness distribution. However, because gravity-driven slope failures are sensitive to variations in slope gradient, they are preferentially accommodated in bathymetrically low regions (Kneller et al., 2016). We therefore suggest that the buried MTCs can exert a primary control on the thickness distribution of subsequent slope failures. Detailed mapping of MTCs is therefore essential in slope failure-prone areas, noting that future subsea construction should avoid areas where seabed MTCs are relatively thin, given this may represent the depocentre for a future MTC (Figure 17).

6. Conclusions

Our study provides a valuable case study on the dynamic interactions and influence between eleven stacked MTCs and enables a better understanding of slope failure mechanisms in passive margins globally. Based on the results of this study, the following conclusions can be drawn:

(1) We reveal that the Kangaroo Syncline accommodate at least eleven large stacked MTCs that comprise nearly 80% of the total stratigraphy. We suggest that the Kangaroo Syncline is particularly prone to slope failure because of the interplay of four factors: widespread and sustained carbonate ooze deposition, the abundance of vertical fluid migration, the lack of seismic strengthening process, and tectonically induced increases in seabed gradient.

(2) We demonstrate that pre-existing MTCs can have far-reaching effects on the stability of the surrounding sediment pile. Potentially, MTC emplacement can trigger differential compaction and headwall scarp effect that influences the bathymetry, distribution and emplacement of subsequent slope failures. More specifically, pre-existing MTCs can affect

lithology composition, provide bathymetric constraints to failure displacement, redirect flow pathways, control runout distances and enhance the erosion capacity of the subsequent slope failures.

(3) Our results demonstrate that buried MTCs exert a significant influence on subsequent slope failure distribution patterns and their depocentre. Therefore, measuring the pre-existing MTCs (especially their top surface) provides a unique analogue for predicting future MTC locations and providing key information for the planning of future seabed infrastructure and hazards mitigation.

Figure Caption

Figure 1. (A) The bathymetric map of the NW Australian region shows the study area location, key tectonic structures, and location of datasets. The location of ODP 762 is marked as a red dot, the Willem 3D seismic is indicated by a red polygon and the 2D seismic data by a solid grey line. (B) Tectonostratigraphic chart for the study area, lithology and age is defined in the ODP 762 report. All data relating to the ODP log is depth below the seabed from ODP site 762. (C) Regional seismic section through the Exmouth Plateau Arch, Kangaroo Syncline and the lower continental slope. Horizon H0 is the base of the study interval and has been tied to the late Miocene Unconformity surface. H0 is equivalent to Reflector 7 of Boyd et al. (1993), N17–1 horizon of Hull and Griffiths (2002), Horizon C of Nugraha et al. (2018), and Horizon H2 of Wu et al. (2023). See Figure 1A for the location of Figure 1C.

Figure 2. (A) The regional seismic section through the Willem 3D shows the study interval and the late Miocene Unconformity surface (H0). (B) Sketches showing the location of stacked MTCs 1-6, undifferentiated MTCs and key seismic horizons (H1-seabed). The location of Figures 2C and 2D is indicated in Figure 2A. (C) Zoomed-in view of the Willem 3D survey

area, showing the locations of Figures 3, 4, and 5 presented in this study. (D) Zoomed-in view of the Willem 3D survey area, showing the locations of Figures 6 and 7 presented in this study.

Figure 3. (A) Variance attribute map calculated on the basal shear surface (H1) of MTC-1, showing the boundaries and internal key structures of the MTC-1. (B) Interpreted sketch of MTC-1, showing the boundaries and internal key structures of the MTC-1. (C) The seismic section cutting through MTC-1 and MTC-2 shows the detailed structures and seismic characters. (D) The seismic section cutting along the transport direction of MTC-1. See Figure 3B for location.

Figure 4. (A) Uninterpreted variance attribute map calculated on the basal shear surface (H3) of MTC-2, showing the boundaries and internal key structures of the MTC-2. (B) Interpreted sketch of MTC-2, showing the MTC boundaries, key kinematic indicators and the transport direction. (C) Isochron (TWT thickness) map of MTC-2, indicating a westward thickness thinning trend. The contour interval is 60 ms. (D) The seismic section cutting through MTC-2 and MTC-3 shows the detailed structures and seismic characters. See the location of this seismic section in Figure 4B.

Figure 5. (A) Uninterpreted variance attribute map calculated on the basal shear surface (H5) of MTC-3, showing the boundaries and internal key structures of the MTC-3. (B) Interpreted sketch of MTC-3, showing its boundaries and key kinematic indicators. (C) Isochron (TWT thickness) map of MTC-3, indicating an eastward thickness thinning trend. The contour interval is 60 ms. (D) The seismic section cuts through the scours of MTC-3, showing the cross-sectional profile of the scours. (E) The seismic section cuts through the eastern margin of MTC-3, showing the thrust terminating against the underlying spread blocks. See the location of the seismic sections in Figure 5B.

Figure 6. (A) Variance attribute map calculated on the basal shear surface (H7) of MTC-4, showing the boundaries and internal key structures of the MTC-4. (B) Spectral decomposition calculated from the basal shear surface of MTC-4, providing a detailed view of the internal fingerprint-like structures and boundaries of this MTC. (C) Interpreted sketch of MTC-4, illustrating external geometry and key kinematic indicators. (D) The seismic section cutting through MTC-4 shows its detailed structure and internal seismic characteristics. The white dashed line marks a flattened surface to better visualize MTC-4, and the white arrow indicates its transport direction. The location of this seismic section is shown in Figure 4C.

Figure 7. (A) Variance attribute map calculated on the basal shear surface (H9) of MTC-5, showing the boundaries and internal key structures. (B) Spectral decomposition calculated from the basal shear surface of MTC-5, showing detailed fingerprint-like internal structures and boundaries. (C) Interpreted sketch of MTC-5, showing the external geometry and internal structural details. (D) The seismic section cutting through MTC-5 shows its detailed structure and internal seismic characteristics. The white dashed line marks a flattened surface to better visualize MTC-5, and the white arrow indicates its transport direction. The location of this seismic section is shown in Figure 5C.

Figure 8. (A) Variance attribute map calculated on the basal shear surface (H11) of MTC-6, showing the boundaries and internal key structures. (B) Interpreted sketch of MTC-6, showing the external geometry and internal structural details. (C) Variance attribute map calculated on the basal shear surface (H13) of MTC-7, showing the boundaries and internal key structures. (D) Interpreted sketch of MTC-7, showing the external geometry and internal structural details.

Figure 9. (A) Bathymetric map calculated on the basal shear surface (H15) of MTC-8, showing the paleoseafloor bathymetry. (B) The uninterpreted variance attribute map calculated on the basal shear surface of MTC-8 shows the MTC's boundaries and internal key structures. (C)

Interpreted sketch of MTC-8, showing the MTCs boundaries and key kinematic indicators. (D) Isochron (TWT thickness) map of MTC-8, the contours are every 60 ms. (E) Seismic section cutting through MTC-8 shows the relief variation near the headwall scarp of MTC-2 and groove details. See the location of the seismic section in Figure 9C.

Figure 10. (A) Seismic section cutting across the grooves of MTC-8, with the basal shear surface shown in 3D view. The location of this seismic section is shown in Figure 9C. (B) Zoom-in view of the protruding structure developed on the basal shear surface of MTC-8, this attribute is attracted 15 ms above the basal shear surface. See location in Figure 9C. (C) Seismic section cut along the dip of the protruding structure, showing the internal seismic facies.

Figure 11. (A) Zoom-in map of Figure 9A, showing directional changes of grooves on the basal shear surface of MTC-8 near a NW-trending lineation. Note the NW-trending lineation corresponds with the headwall scarp of MTD-2, lying below. The location of Figure 11A is shown in Figure 9C. (B) Zoom-in view illustrate the width and incision depth of G-1 in cross-section. Groove width was measured between opposing flanks, while incision depth was taken from the groove base to the reference level defined by the undeformed basal shear surface. (C) Zoom-in view and the cross-sectional geometry at the groove termination. (D) The Rose diagram shows the orientation of the grooves, blue indicates grooves developed outside the NW-trending lineation, and red indicates grooves developed within the NW-trending lineation. (E) The width and incision depth of groove G-1, see the location of groove G-1 in Figure 11A.

Figure 12. 3D view of MTC-8's basal shear surface, showing a well-developed field of grooves. The extent of this figure is the same as in Figure 11A, but the viewing angle is rotated 180° counterclockwise.

Figure 13. (A) Uninterpreted variance attribute map calculated on the basal shear surface (H17) of MTC-9, showing the boundaries and internal key structures of the MTC-9. (B) Interpreted

sketch of MTC-9, showing the boundaries, headwall scarp, internal blocks and other kinematic indicators of this MTC. (C) Isochron (TWT thickness) map of MTC-9, revealing a thick-thin-thick tripartite pattern. (D) Bathymetric map calculated on the top surface (H18) of MTC-9, showing the block associated paleoseabed bathymetry.

Figure 14. (A) Zoomed-in view of the basal shear surface of MTC-9, showing NNW-trending scours. The location of Figure 14A is indicated in Figure 13A. (B) Zoomed-in view of the top surface of MTC-9, showing the tips of intruding blocks on the paleoseabed. The location of Figure 14B is indicated in Figure 13D. (C) Seismic dip section along the scours, showing the internal seismic facies of megaclasts and the rugged top surface of MTC-9. (D) Seismic cross section along the scours, showing the internal seismic facies of megaclasts and the rugged top surface of MTC-9. See the locations of seismic section in Figure 14A.

Figure 15. (A) Zoomed-in view of the basal shear surface of MTC-9, showing transported blocks near the headwall scarp. The location of Figure 15A is indicated in Figure 13A. (B) The seismic section crosses the area of the headwall scarp and translated blocks of the MTC-9. Note the basal shear surface's step-shaped geometry near the headwall and the rugged top surfaces. (C) Seismic section across transported blocks, showing their internal seismic characteristics and rugged top surfaces. The locations of Figures 15B and 15C are indicated in Figure 15A. (D) Seismic section cutting across the remnant block, showing its boundary and internal seismic facies. The location of this seismic section is shown in Figure 13B.

Figure 16. (A) The variance attribute map calculated on the basal shear surface (H19) of MTC-10 shows the MTC's boundaries and internal key structures. (B) Isochron (TWT thickness) map of MTC-10, showing the depocentre of the MTC-10. (C) The variance attribute map calculated on the basal shear surface (H21) of MTC-11 shows the MTC's boundaries and internal key

structures. (B) Isochron (TWT thickness) map of MTC-11, showing the depocentre of the MTC-11.

Figure 17. (A) Seismic cross section cutting across the MTC-10 and MTC-11, showing the thickness of these MTCs pinch-out at the local topography high created by the underlying MTC-9. See the location in Figure 16A. (B) Seismic dip section cutting across the central frontally confined domain of MTC-11, showing that MTC-11 terminates against blocks within the underlying MTC-9. (C) Seismic dip section cutting across the frontally emergent domain of MTC-11, showing that MTC-11 was able to transport downslope without obstruction where underlying blocks are absent in MTC-9. The locations of Figures 17B and 17C are indicated in Figure 16C.

Figure 18. The composite diagram of the MTCs thickness relationships, notes that the Y axis stands for thickness in time, and the X axis indicates the length in kilometres. Generally, younger MTCs thicken in areas where older MTCs are relatively thinner, and vice versa.

Figure 19. (A) Shear strength degradation of carbonate oozes during cyclic T-bar penetrometer tests, modified from Gaudin and White (2009). The loss of strength is expressed as the ratio of the remoulded shear strength to the intact shear strength, experienced by different soils during cycles of remoulding for siliciclastic sediments and carbonate oozes of the offshore NW Australia. (B) Undrained shear strength measurements from the Ocean Drilling Program and Integrated Ocean Drilling Program. Nine type sites are chosen from the top 100 m below seabed sediment and are normally consolidated on active and passive margins. Active margin sites include offshore Japan (Site C0001), Cascadia (Site U1329), and two sites offshore Costa Rica (Sites 1039 and U1414). Passive margin sites include Amazon Fan (Site 942), Madeira abyssal plain (Site 951), New Jersey (Site 1073), Carolina Slope (Site 1054), and Exmouth Plateau and Kangaroo Syncline (ODP 762). The shear strength of the carbonate ooze in the Kangaroo

Syncline is lower than that of siliciclastic sediments on other passive margins, and that is significantly lower than that of siliciclastic sediments on active margins. Data sets for this figure are adopted from the global survey of Sawyer and DeVore (2015). Black and red dotted lines are the average undrained shear strength for passive and active margins, respectively.

Acknowledgements

The first author thanks financial support from the National Natural Science Foundation of China (Grant No. 42406060), the Natural Science Foundation of Shanghai (Grant No. 23ZR1467800), and the Fundamental Research Funds for the Central Universities, China. We thank Michael A. Clare, Wei Li and Song Jing for helpful discussions while preparing the manuscript. The first author also thanks Zhenghao Han and Huiting Wang for there assistance in figure preparation. We acknowledge the value of the "open data" policy from Geoscience Australia (https://www.ga.gov.au/data-pubs) and thank them for providing the seismic reflection data. This study used the Willem 3D and the Willem 2D seismic surveys. The GEBCO_2021 bathymetry map is downloaded from https://www.ngdc.noaa.gov/maps/autogrid/. Data for the shear strength measurements are adopted from Supporting Information S1 of Sawyer and DeVore (2015), which can be downloaded from https://agupubs.onlinelibrary.wiley.com/doi/full/10.1002/2015GL066603.

References

Dott Jr, R., 1963, Dynamics of subaqueous gravity depositional processes: AAPG Bulletin, v. 47, no. 1, p. 104-128.

Nardin, T. R., Hein, F., Gorsline, D. S., and Edwards, B., 1979, A review of mass movement processes sediment and acoustic characteristics, and contrasts in slope and base-of-slope systems versus canyon-fan-basin floor systems.

Barber, P., 1988, The Exmouth Plateau deep water frontier: a case history.

Nemec, W., 1990, Aspects of sediment movement on steep delta slopes: Coarse-grained deltas, v. 10, p. 29-73.

Exon, N., Haq, B., and Von Rad, U., Exmouth Plateau revisited: scientific drilling and geological framework, *in* Proceedings Proceedings of the Ocean Drilling Program, Scientific Results1992, Volume 122, Ocean Drilling Program College Station, Tex, p. 3-20.

Haq, B. U., Boyd, R. L., Exon, N. F., and von Rad, U., 1992, 47. EVOLUTION OF THE CENTRAL EXMOUTH PLATEAU: A POST-DRILLING PERSPECTIVE1.

Palmer-Julson, A., and Rack, F., 1992, The relationship between sediment fabric and planktonic microfossil taphonomy: how do plankton skeletons become pelagic ooze?: Palaios, p. 167-177.

von Rad, U., Haq, B.U., et al., 1992, Proceedings of the Ocean Program, Scientific Results: Ocean Drilling Program, v. Leg 122.

Boyd, R., Williamson, P., and Haq, B., 1993, Seismic Stratigraphy and Passive ‐ Margin Evolution of the Southern Exmouth Plateau: Sequence Stratigraphy and Facies Associations, p. 579-603.

Rack, F. R., Bryant, W. R., and Julson, A. P., 1993, Microfabric and physical properties of deep-sea high latitude carbonate oozes, Carbonate Microfabrics, Springer, p. 129-147.

Piper, D., Pirmez, C., Manley, P., Long, D., Flood, R., Normark, W., and Showers, W., Mass-transport deposits of the Amazon Fan, *in* Proceedings PROCEEDINGS-OCEAN DRILLING PROGRAM SCIENTIFIC RESULTS1997, NATIONAL SCIENCE FOUNDATION, p. 109-146.

Keep, M., Powell, C. M., and Baillie, P., 1998, Neogene deformation of the North West Shelf, Australia.

Tindale, K., Newell, N., Keall, J., Smith, N., Purcell, P., and Purcell, R., 1998, Structural evolution and charge history of the Exmouth Sub-basin, northern Carnarvon Basin, Western Australia: The sedimentary basins of Western Australia, v. 2.

Nissen, S. E., Haskell, N. L., Steiner, C. T., and Coterill, K. L., 1999, Debris flow outrunner blocks, glide tracks, and pressure ridges identified on the Nigerian continental slope using 3-D seismic coherency: The Leading Edge, v. 18, no. 5, p. 595-599.

Partyka, G., Gridley, J., and Lopez, J., 1999, Interpretational applications of spectral decomposition in reservoir characterization: The leading edge, v. 18, no. 3, p. 353-360.

Piper, D. J., Cochonat, P., and Morrison, M. L., 1999, The sequence of events around the epicentre of the 1929 Grand Banks earthquake: initiation of debris flows and turbidity current inferred from sidescan sonar: Sedimentology, v. 46, no. 1, p. 79-97.

Tanaka, H., and Locat, J., 1999, A microstructural investigation of Osaka Bay clay: the impact of microfossils on its mechanical behaviour: Canadian Geotechnical Journal, v. 36, no. 3, p. 493-508.

Driscoll, N. W., Weissel, J. K., and Goff, J. A., 2000, Potential for large-scale submarine slope failure and tsunami generation along the US mid-Atlantic coast: Geology, v. 28, no. 5, p. 407-410.

Van Bemmel, P. P., and Pepper, R. E., 2000, Seismic signal processing method and apparatus for generating a cube of variance values, Google Patents.

Hull, J., and Griffiths, C., 2002, Sequence stratigraphic evolution of the Albian to Recent section of the Dampier Sub-basin, North West Shelf, Australia: PhD thesis 1999. University of Adelaide, Australia.

Longley, I., Buessenschuett, C., Clydsdale, L., Cubitt, C., Davis, R., Johnson, M., Marshall, N., Murray, A., Somerville, R., and Spry, T., The North West Shelf of Australia—a Woodside perspective, *in* Proceedings The Sedimentary Basins of Western Australia 3: Proceedings of the Petroleum Exploration Society of Australia Symposium, Perth2002, Pet. Explor. Soc. of Aust. Perth, p. 27-88.

Posamentier, H. W., and Kolla, V., 2003, Seismic geomorphology and stratigraphy of depositional elements in deep-water settings: Journal of sedimentary research, v. 73, no. 3, p. 367-388.

Sultan, N., Cochonat, P., Foucher, J., Mienert, J., Haflidason, H., and Sejrup, H., 2003, Effect of gas hydrates dissociation on seafloor slope stability, Submarine mass movements and their consequences, Springer, p. 103-111.

Volpi, V., Camerlenghi, A., Hillenbrand, C. D., Rebesco, M., and Ivaldi, R., 2003, Effects of biogenic silica on sediment compaction and slope stability on the Pacific margin of the Antarctic Peninsula: Basin Research, v. 15, no. 3, p. 339-363.

Shipp, R. C., 2004, Physical Characteristics and Impact of Mass Transport Complexes on Deepwater Jetted Conductors and Suction Anchor Piles.

Bryn, P., Berg, K., Forsberg, C. F., Solheim, A., and Kvalstad, T. J., 2005, Explaining the Storegga slide: Marine and Petroleum Geology, v. 22, no. 1, p. 11-19.

Bünz, S., Mienert, J., Bryn, P., and Berg, K., 2005, Fluid flow impact on slope failure from 3D seismic data: a case study in the Storegga Slide: Basin Research, v. 17, no. 1, p. 109-122.

Frey Martinez, J., Cartwright, J., and Hall, B., 2005, 3D seismic interpretation of slump complexes: examples from the continental margin of Israel: Basin Research, v. 17, no. 1, p. 83-108.

Gee, M., Gawthorpe, R., and Friedmann, J., 2005, Giant striations at the base of a submarine landslide: Marine Geology, v. 214, no. 1-3, p. 287-294.

Kvalstad, T. J., Andresen, L., Forsberg, C. F., Berg, K., Bryn, P., and Wangen, M., 2005, The Storegga slide: evaluation of triggering sources and slide mechanics: Marine and Petroleum Geology, v. 22, no. 1, p. 245-256.

Solheim, A., Berg, K., Forsberg, C., and Bryn, P., 2005, The Storegga Slide complex: repetitive large scale sliding with similar cause and development: Marine and Petroleum Geology, v. 22, no. 1-2, p. 97-107.

Strout, J. M., and Tjelta, T. I., 2005, In situ pore pressures: What is their significance and how can they be reliably measured?: Marine and Petroleum Geology, v. 22, no. 1-2, p. 275-285.

Cathro, D. L., and Karner, G. D., 2006, Cretaceous–Tertiary inversion history of the Dampier Sub-Basin, Northwest Australia: insights from quantitative basin modelling: Marine and Petroleum Geology, v. 23, no. 4, p. 503-526.

Davies, R. J., and Clark, I. R., 2006, Submarine slope failure primed and triggered by silica and its diagenesis: Basin Research, v. 18, no. 3, p. 339-350.

Frey-Martínez, J., Cartwright, J., and James, D., 2006, Frontally confined versus frontally emergent submarine landslides: a 3D seismic characterisation: Marine and Petroleum Geology, v. 23, no. 5, p. 585-604.

Masson, D., Harbitz, C., Wynn, R., Pedersen, G., and Løvholt, F., 2006, Submarine landslides: processes, triggers and hazard prediction: Philosophical Transactions of the Royal Society A: Mathematical, Physical and Engineering Sciences, v. 364, no. 1845, p. 2009-2039.

Moscardelli, L., Wood, L., and Mann, P., 2006, Mass-transport complexes and associated processes in the offshore area of Trinidad and Venezuela: AAPG bulletin, v. 90, no. 7, p. 1059-1088.

Sawyer, D. E., 2007, Lateral Variations in Core, Log, and Seismic Attributes of a Mass Transport Complex in the Ursa Region, IODP Expedition 308, Northern Gulf of Mexico.

Bull, S., Cartwright, J., and Huuse, M., 2009, A review of kinematic indicators from mass-transport complexes using 3D seismic data: Marine and Petroleum Geology, v. 26, no. 7, p. 1132-1151.

Gaudin, C., and White, D., 2009, New centrifuge modelling techniques for investigating seabed pipeline behaviour.

Sawyer, D. E., Flemings, P. B., Dugan, B., and Germaine, J. T., 2009, Retrogressive failures recorded in mass transport deposits in the Ursa Basin, Northern Gulf of Mexico: Journal of Geophysical Research: Solid Earth, v. 114, no. B10.

Alves, T. M., 2010, 3D Seismic examples of differential compaction in mass-transport deposits and their effect on post-failure strata: Marine Geology, v. 271, no. 3-4, p. 212-224.

Alves, T. M., and Cartwright, J. A., 2010, The effect of mass-transport deposits on the younger slope morphology, offshore Brazil: Marine and Petroleum Geology, v. 27, no. 9, p. 2027-2036.

Lawrence, G. W., and Cartwright, J. A., 2010, The stratigraphic and geographic distribution of giant craters and remobilised sediment mounds on the mid Norway margin, and their relation to long term fluid flow: Marine and Petroleum Geology, v. 27, no. 4, p. 733-747.

Masson, D., Wynn, R., and Talling, P., 2010, Large landslides on passive continental margins: processes, hypotheses and outstanding questions, Submarine mass movements and their consequences, Springer, p. 153-165.

Jackson, C. A., 2011, Three-dimensional seismic analysis of megaclast deformation within a mass transport deposit; implications for debris flow kinematics: Geology, v. 39, no. 3, p. 203-206.

Moernaut, J., and De Batist, M., 2011, Frontal emplacement and mobility of sublacustrine landslides: results from morphometric and seismostratigraphic analysis: Marine Geology, v. 285, no. 1-4, p. 29-45.

Nelson, C. H., Escutia, C., Damuth, J. E., and Twichell, D., 2011, Interplay of mass-transport and turbidite-system deposits in different active tectonic and passive continental margin settings: external and local controlling factors: Sediment. Geol, v. 96, p. 39-66.

Posamentier, H. W., and Martinsen, O. J., 2011, The character and genesis of submarine mass-transport deposits: insights from outcrop and 3D seismic data: Mass-transport deposits in deepwater settings: Society for Sedimentary Geology (SEPM) Special Publication 96, p. 7-38.

Berndt, C., Costa, S., Canals, M., Camerlenghi, A., de Mol, B., and Saunders, M., 2012, Repeated slope failure linked to fluid migration: the Ana submarine landslide complex, Eivissa Channel, Western Mediterranean Sea: Earth and Planetary Science Letters, v. 319, p. 65-74.

Hengesh, J., Dirstein, J. K., and Stanley, A. J., 2012, Seafloor geomorphology and submarine landslide hazards along the continental slope in the Carnarvon Basin, Exmouth Plateau, North West Shelf, Australia: The APPEA Journal, v. 52, no. 1, p. 493-512.

Ilg, B. R., Hemmings-Sykes, S., Nicol, A., Baur, J., Fohrmann, M., Funnell, R., and Milner, M., 2012, Normal faults and gas migration in an active plate boundary, southern Taranaki Basin, offshore New Zealand: AAPG bulletin, v. 96, no. 9, p. 1733-1756.

Albini, P., Musson, R., Gomez Capera, A., Locati, M., Rovida, A., Stucchi, M., and Viganò, D., 2013, Global historical earthquake archive and catalogue (1000-1903): Pavia, Italy.

Hengesh, J., Dirstein, J., and Stanley, A., 2013, Landslide geomorphology along the Exmouth plateau continental margin, North West Shelf, Australia: Australian Geomechanics Journal, v. 48, no. 4, p. 71-92.

Scarselli, N., McClay, K., and Elders, C., 2013, Submarine slide and slump complexes, Exmouth Plateau, NW Shelf of Australia, *in* Proceedings The Sedimentary Basins of Western Australia IV: Proceedings of the Petroleum Exploration Society of Australia Symposium, Perth, WA2013a, Volume 18.

-, Submarine slide and slump complexes, Exmouth Plateau, NW Shelf of Australia, *in* Proceedings The Sedimentary Basins of Western Australia IV: Proceedings of the Petroleum Exploration Society of Australia Symposium, Perth, WA2013b.

Harbitz, C. B., Løvholt, F., and Bungum, H., 2014, Submarine landslide tsunamis: how extreme and how likely?: Natural Hazards, v. 72, no. 3, p. 1341-1374.

Li, W., Wu, S., Wang, X., Zhao, F., Wang, D., Mi, L., and Li, Q., Baiyun slide and its relation to fluid migration in the northern slope of Southern China Sea, *in* Proceedings Submarine mass movements and their consequences: 6th International Symposium2014, Springer, p. 105-115.

Talling, P. J., CLARE, M. L., Urlaub, M., Pope, E., Hunt, J. E., and Watt, S. F., 2014, Large submarine landslides on continental slopes: geohazards, methane release, and climate change: Oceanography, v. 27, no. 2, p. 32-45.

Li, W., Alves, T. M., Wu, S., Völker, D., Zhao, F., Mi, L., and Kopf, A., 2015, Recurrent slope failure and submarine channel incision as key factors controlling reservoir potential in the South China Sea (Qiongdongnan Basin, South Hainan Island): Marine and Petroleum Geology, v. 64, p. 17-30.

Sawyer, D. E., and DeVore, J. R., 2015, Elevated shear strength of sediments on active margins: Evidence for seismic strengthening: Geophysical Research Letters, v. 42, no. 23, p. 10,216-210,221.

Sharman, G. R., Graham, S. A., Masalimova, L. U., Shumaker, L. E., and King, P. R., 2015, Spatial patterns of deformation and paleoslope estimation within the marginal and central portions of a basin-floor mass-transport deposit, Taranaki Basin, New Zealand: Geosphere, v. 11, no. 2, p. 266-306.

Urlaub, M., Talling, P. J., Zervos, A., and Masson, D., 2015, What causes large submarine landslides on low gradient (< 2°) continental slopes with slow (∼ 0.15 m/kyr) sediment accumulation?: Journal of Geophysical Research: Solid Earth, v. 120, no. 10, p. 6722-6739.

Aqrawi, A. A., and Bø, T. H., 2016, Amplitude contrast seismic attribute, Google Patents.

DeVore, J. R., and Sawyer, D. E., 2016, Shear strength of siliciclastic sediments from passive and active margins (0–100 m below seafloor): insights into seismic strengthening, Submarine Mass Movements and their Consequences, Springer, p. 173-180.

Kneller, B., Dykstra, M., Fairweather, L., and Milana, J. P., 2016, Mass-transport and slope accommodation: Implications for turbidite sandstone reservoirs: AAPG Bulletin, v. 100, no. 2, p. 213-235.

Moscardelli, L., and Wood, L., 2016, Morphometry of mass-transport deposits as a predictive tool: Bulletin, v. 128, no. 1-2, p. 47-80.

Reis, A., Araújo, E., Silva, C., Cruz, A., Gorini, C., Droz, L., Migeon, S., Perovano, R., King, I., and Bache, F., 2016, Effects of a regional décollement level for gravity tectonics on late Neogene to recent large-scale slope instabilities in the Foz do Amazonas Basin, Brazil: Marine and Petroleum Geology, v. 75, p. 29-52.

Schnyder, J. S., Eberli, G. P., Kirby, J. T., Shi, F., Tehranirad, B., Mulder, T., Ducassou, E., Hebbeln, D., and Wintersteller, P., 2016, Tsunamis caused by submarine slope failures along western Great Bahama Bank: Scientific reports, v. 6, no. 1, p. 35925.

Ten Brink, U. S., Andrews, B. D., and Miller, N. C., 2016, Seismicity and sedimentation rate effects on submarine slope stability: Geology, v. 44, no. 7, p. 563-566.

Covault, J. A., Kostic, S., Paull, C. K., Sylvester, Z., and Fildani, A., 2017, Cyclic steps and related supercritical bedforms: building blocks of deep-water depositional systems, western North America: Marine Geology, v. 393, p. 4-20.

Gavey, R., Carter, L., Liu, J. T., Talling, P. J., Hsu, R., Pope, E., and Evans, G., 2017, Frequent sediment density flows during 2006 to 2015, triggered by competing seismic and weather events: Observations from subsea cable breaks off southern Taiwan: Marine Geology, v. 384, p. 147-158.

Pope, E. L., Talling, P. J., Carter, L., Clare, M. A., and Hunt, J. E., 2017, Damaging sediment density flows triggered by tropical cyclones: Earth and Planetary Science Letters, v. 458, p. 161-169.

Rusconi, F. J., 2017, 3D seismic interpretation of a Plio-Pleistocene mass transport deposit in the deepwater Taranaki Basin of New Zealand, University of Arkansas.

Safadi, M., Meilijson, A., and Makovsky, Y., 2017, Internal deformation of the southeast Levant margin through continued activity of buried mass transport deposits: Tectonics, v. 36, no. 3, p. 559-581.

Hodgson, D., Brooks, H., Ortiz-Karpf, A., Spychala, Y., Lee, D., and Jackson, C.-L., 2018, Entrainment and abrasion of megaclasts during submarine landsliding and their impact on flow behaviour: Geological Society, London, Special Publications, v. 477, p. SP477. 426.

Nugraha, H. D., Jackson, C. A. L., Johnson, H. D., Hodgson, D. M., and Reeve, M. T., 2018, Tectonic and oceanographic process interactions archived in Late Cretaceous to Present deep‐marine stratigraphy on the Exmouth Plateau, offshore NW Australia: Basin Research.

Sobiesiak, M. S., Kneller, B., Alsop, G. I., and Milana, J. P., 2018, Styles of basal interaction beneath mass transport deposits: Marine and Petroleum Geology, v. 98, p. 629-639.

Sun, Q., Alves, T. M., Lu, X., Chen, C., and Xie, X., 2018, True volumes of slope failure estimated from a Quaternary mass‐transport deposit in the northern South China Sea: Geophysical Research Letters, v. 45, no. 6, p. 2642-2651.

Ward, N. I., Alves, T. M., and Blenkinsop, T. G., 2018, Submarine sediment routing over a blocky mass‐transport deposit in the Espírito Santo Basin, SE Brazil: Basin Research, v. 30, no. 4, p. 816-834.

Franzel, M., and Back, S., 2019, Three-dimensional seismic sedimentology and stratigraphic architecture of prograding clinoforms, central Taranaki Basin, New Zealand: International Journal of Earth Sciences, v. 108, no. 2, p. 475-496.

Kioka, A., Schwestermann, T., Moernaut, J., Ikehara, K., Kanamatsu, T., McHugh, C., dos Santos Ferreira, C., Wiemer, G., Haghipour, N., and Kopf, A., 2019, Megathrust earthquake drives drastic organic carbon supply to the hadal trench: Scientific reports, v. 9, no. 1, p. 1553.

Lintern, D. G., Mosher, D., Moscardelli, L., Bobrowsky, P., Campbell, C., Chaytor, J., Clague, J., Georgiopoulou, A., Lajeunesse, P., and Normandeau, A., Subaqueous mass movements and their consequences: Assessing geohazards, environmental implications and economic significance of subaqueous landslides2019, Geological Society of London.

Omeru, T., and Cartwright, J. A., 2019, The efficacy of kinematic indicators in a complexly deformed mass transport deposit: insights from the deepwater Taranaki Basin, New Zealand: Marine and Petroleum Geology, v. 106, p. 74-87.

Paganoni, M., King, J. J., Foschi, M., Mellor-Jones, K., and Cartwright, J. A., 2019, A natural gas hydrate system on the Exmouth Plateau (NW shelf of Australia) sourced by thermogenic hydrocarbon leakage: Marine and Petroleum Geology, v. 99, p. 370-392.

Steventon, M. J., Jackson, C. A. L., Hodgson, D. M., and Johnson, H. D., 2019, Strain analysis of a seismically imaged mass‐transport complex, offshore Uruguay: Basin Research, v. 31, no. 3, p. 600-620.

Velayatham, T., Holford, S., Bunch, M., King, R., and Magee, C., 2019, 3D Seismic Analysis of Ancient Subsurface Fluid Flow in the Exmouth Plateau, Offshore Western Australia.

Watkinson, I. M., and Hall, R., 2019, Impact of communal irrigation on the 2018 Palu earthquake-triggered landslides: Nature Geoscience, v. 12, no. 11, p. 940-945.

Zhao, R., Chen, S., Olariu, C., Steel, R., Zhang, J., and Wang, H., 2019, A model for oblique accretion on the South China Sea margin; Red River (Song Hong) sediment transport into Qiongdongnan Basin since Upper Miocene: Marine Geology, v. 416, p. 106001.

Chen, S., Steel, R., Wang, H., Zhao, R., and Olariu, C., 2020, Clinoform growth and sediment flux into late Cenozoic Qiongdongnan shelf margin, South China Sea: Basin Research, v. 32, no. Clinoforms and Clinothems: Fundamental Elements of Basin Infill, p. 302-319.

Nugraha, H. D., Jackson, C. A.-L., Johnson, H. D., and Hodgson, D. M., 2020, Lateral variability in strain along the toewall of a mass transport deposit: a case study from the Makassar Strait, offshore Indonesia: Journal of the Geological Society, v. 177, no. 6, p. 1261-1279.

Nwoko, J., Kane, I., and Huuse, M., 2020, Megaclasts within mass-transport deposits: Their origin, characteristics and effect on substrates and succeeding flows: Geological Society, London, Special Publications, v. 500, no. 1, p. 515-530.

Peakall, J., Best, J., Baas, J. H., Hodgson, D. M., Clare, M. A., Talling, P. J., Dorrell, R. M., and Lee, D. R., 2020, An integrated process‐based model of flutes and tool marks in deep‐water environments: Implications for palaeohydraulics, the Bouma sequence and hybrid event beds: Sedimentology, v. 67, no. 4, p. 1601-1666.

Barrett, R., Bellwald, B., Talling, P., Micallef, A., Gross, F., Berndt, C., Planke, S., Myklebust, R., and Krastel, S., 2021, Does retrogression always account for the large volume of submarine megaslides? Evidence to the contrary from the Tampen Slide, offshore Norway: Journal of Geophysical Research: Solid Earth, v. 126, no. 2, p. e2020JB020655.

Fildani, A., Kostic, S., Covault, J. A., Maier, K. L., Caress, D. W., and Paull, C. K., 2021, Exploring a new breadth of cyclic steps on distal submarine fans: Sedimentology, v. 68, no. 4, p. 1378-1399.

Gatter, R., Clare, M., Kuhlmann, J., and Huhn, K., 2021, Characterisation of weak layers, physical controls on their global distribution and their role in submarine landslide formation: Earth-Science Reviews, v. 223, p. 103845.

Wu, N., Jackson, C. A.-L., Johnson, H. D., and Hodgson, D. M., 2021a, Lithological, petrophysical, and seal properties of mass-transport complexes, northern Gulf of Mexico: AAPG Bulletin, v. 105, no. 7, p. 1461-1489.

Wu, N., Jackson, C. A. L., Johnson, H. D., Hodgson, D. M., Clare, M. A., Nugraha, H. D., and Li, W., 2021b, The formation and implications of giant blocks and fluid escape structures in submarine lateral spreads: Basin Research.

Abu, C., Jackson, C. A.-L., and Francis, M., 2022, Strike-slip overprinting of initial co-axial shortening within the toe region of a submarine landslide and a model for basal shear surface growth: a case study from the Angoche Basin, offshore Mozambique: Journal of the Geological Society, v. 179, no. 2.

Li, S., Alves, T. M., Li, W., Wang, X., Rebesco, M., Li, J., Zhao, F., Yu, K., and Wu, S., 2022, Morphology and evolution of submarine canyons on the northwest South China Sea margin: Marine Geology, v. 443, p. 106695.

Nugraha, H. D., Jackson, C. A.-L., Johnson, H. D., Hodgson, D. M., and Clare, M. A., 2022, Extreme erosion by submarine slides: Geology, v. 50, no. 10, p. 1130-1134.

Wu, N., Jackson, C. A.-L., Clare, M. A., Hodgson, D. M., Nugraha, H. D., Steventon, M. J., and Zhong, G., 2023, Diagenetic priming of submarine landslides in ooze-rich substrates: Geology, v. 51, no. 1, p. 85-90.

Bellwald, B., Manton, B., Lebedeva-Ivanova, N., Zastrozhnov, D., Myklebust, R., Planke, S., Forsberg, C. F., Vanneste, M., and Locat, J., 2024, Rapid glacial sedimentation and overpressure in oozes causing large craters on the mid-Norwegian margin: integrated interpretation of the Naust, Kai and Brygge formations.

Figure 1

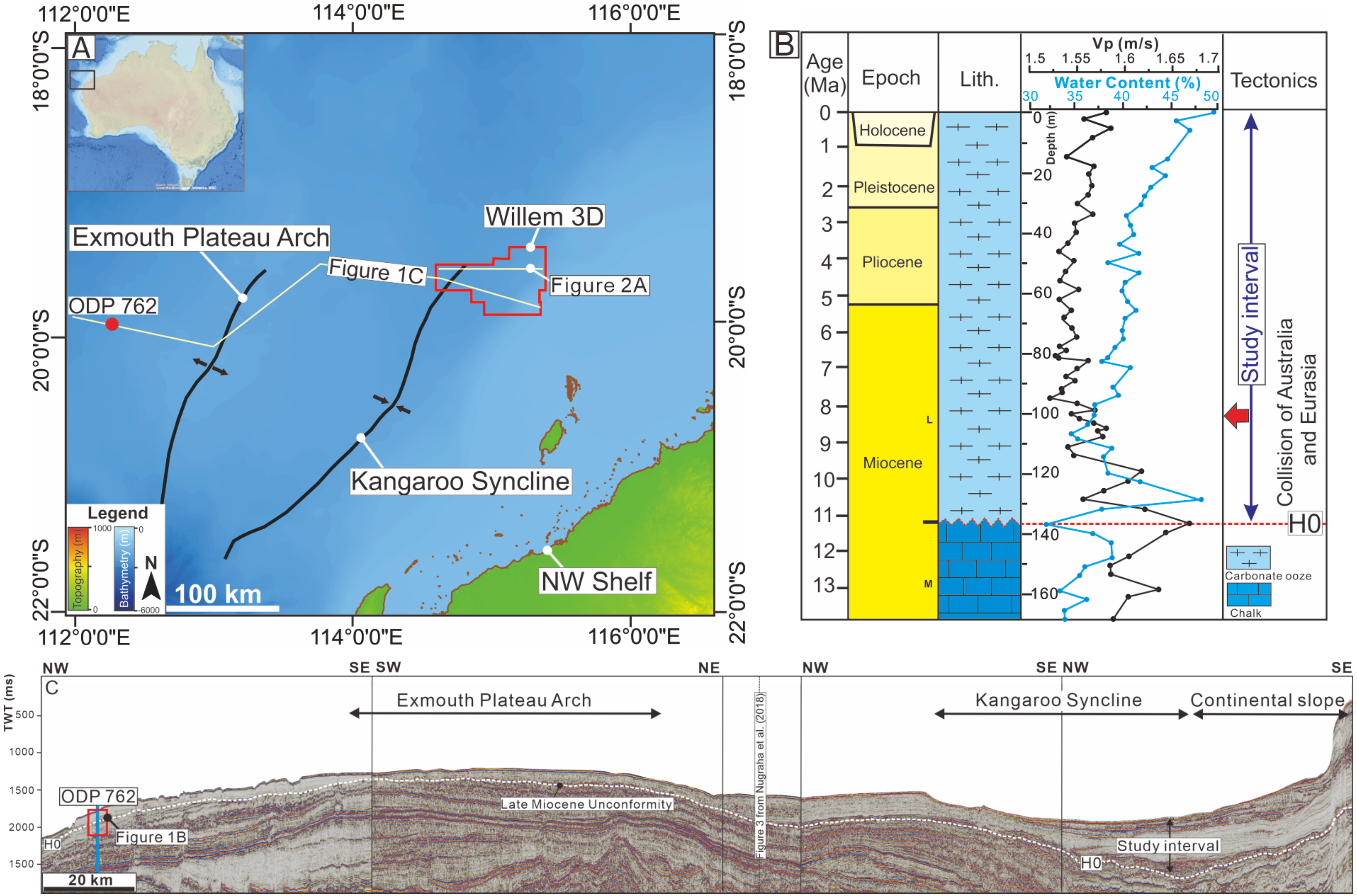
A
112°0'0"E
114°0'0"E
116°0'0"E
18°0'0"S
20°0'0"S
22°0'0"S
Exmouth Plateau Arch
Willem 3D
Figure 1C
Figure 2A
ODP 762
Kangaroo Syncline
NW Shelf
Legend
Topography (m)
1000
0
Bathymetry (m)
0
-6000
N
100 km
B
Age (Ma)
Epoch
Lith.
Vp (m/s)
1.5
1.55
1.6
1.65
1.7
Water Content (%)
30
35
40
45
50
Tectonics
Holocene
Pleistocene
Pliocene
Miocene
L
M
Depth (m)
0
-20
-40
-60
-80
-100
-120
-140
-160
0
1
2
3
4
5
6
7
8
9
10
11
12
13
Study interval
Collision of Australia and Eurasia
H0
Carbonate ooze
Chalk
C
TWT (ms)
500
1000
1500
2000
1500
NW
SE SW
NE
NW
SE NW
SE
Exmouth Plateau Arch
Kangaroo Syncline
Continental slope
ODP 762
Figure 1B
H0
Late Miocene Unconformity
Figure 3 from Nugraha et al. (2018)
Study interval
H0
20 km

Figure 2

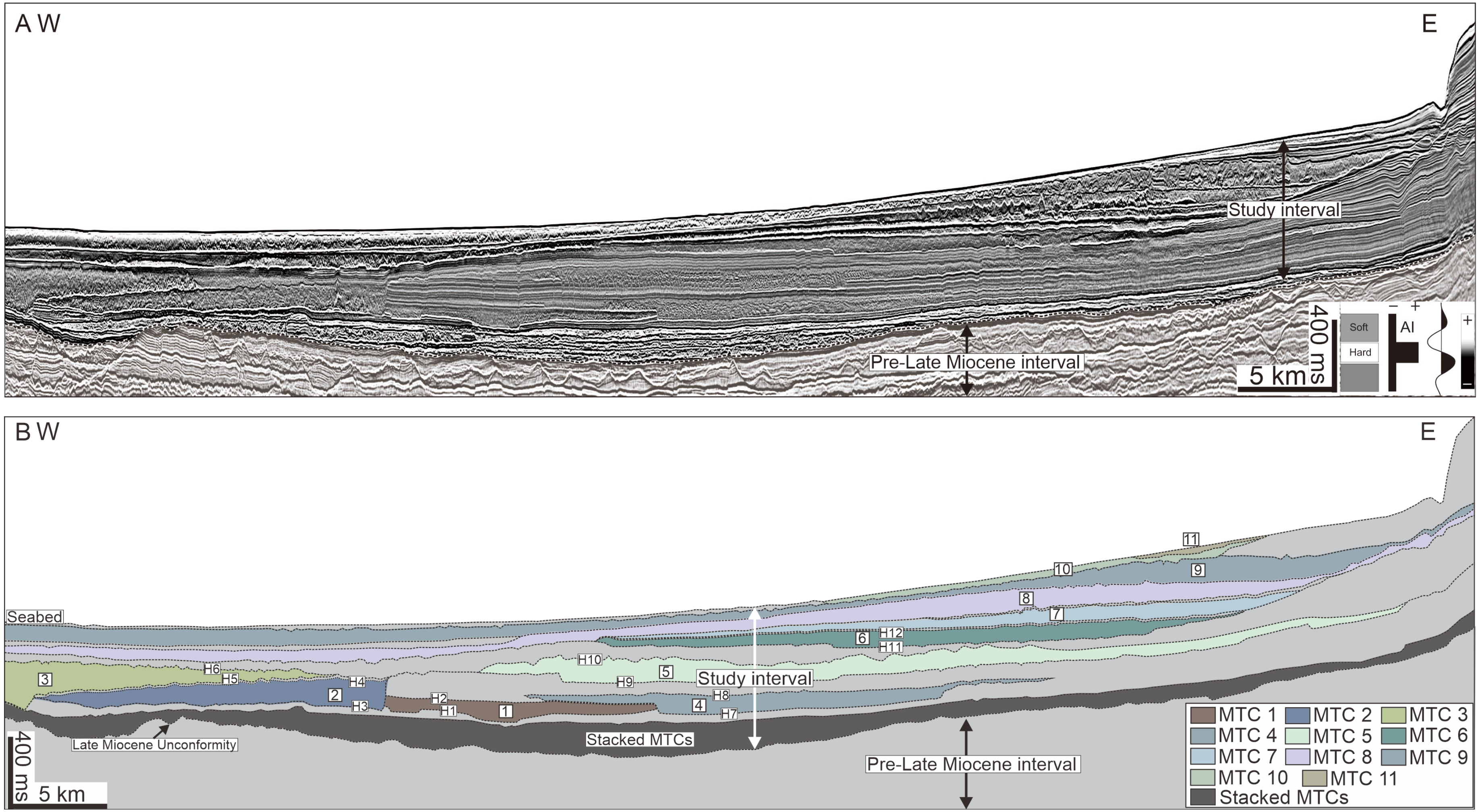
A W
E
Study interval
Pre-Late Miocene interval
400 ms
5 km
Soft
Hard
AI
-
+
+
-
B W
E
Seabed
11
10
9
8
7
6
H12
H11
H10
5
H9
Study interval
3
H6
H5
H4
2
H3
H2
H1
1
4
H8
H7
Late Miocene Unconformity
Stacked MTCs
Pre-Late Miocene interval
400 ms
5 km
MTC 1
MTC 2
MTC 3
MTC 4
MTC 5
MTC 6
MTC 7
MTC 8
MTC 9
MTC 10
MTC 11
Stacked MTCs

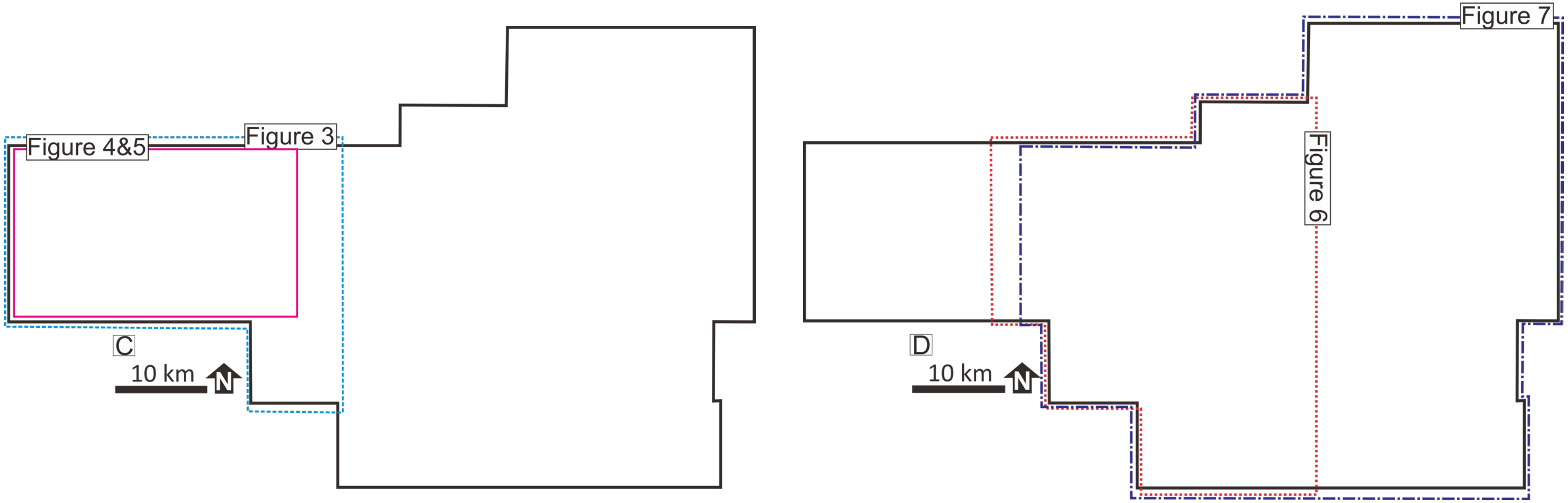
Figure 4&5
Figure 3
C
10 km
N
Figure 7
Figure 6
D
10 km
N

Figure 3: MTC-1

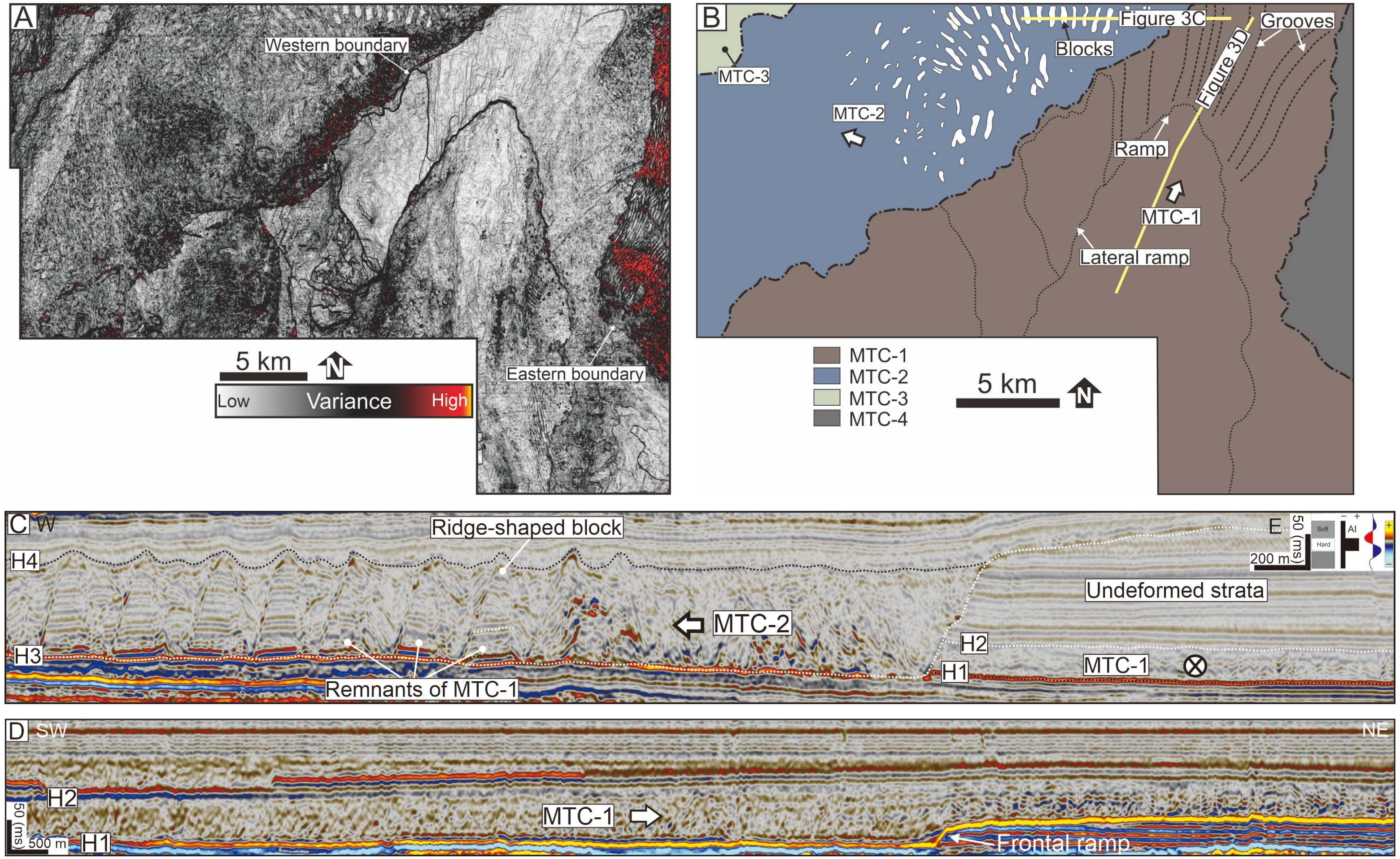

Figure 4: MTC-2

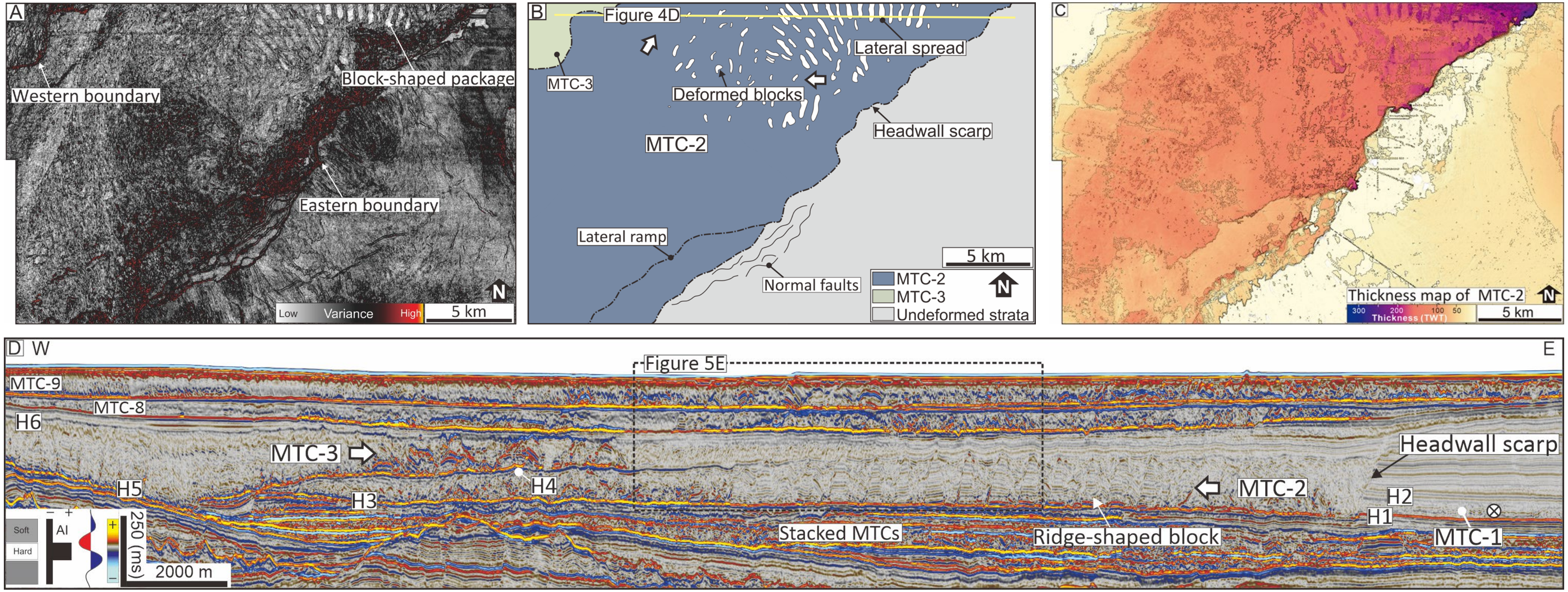

Figure 5: MTC-3

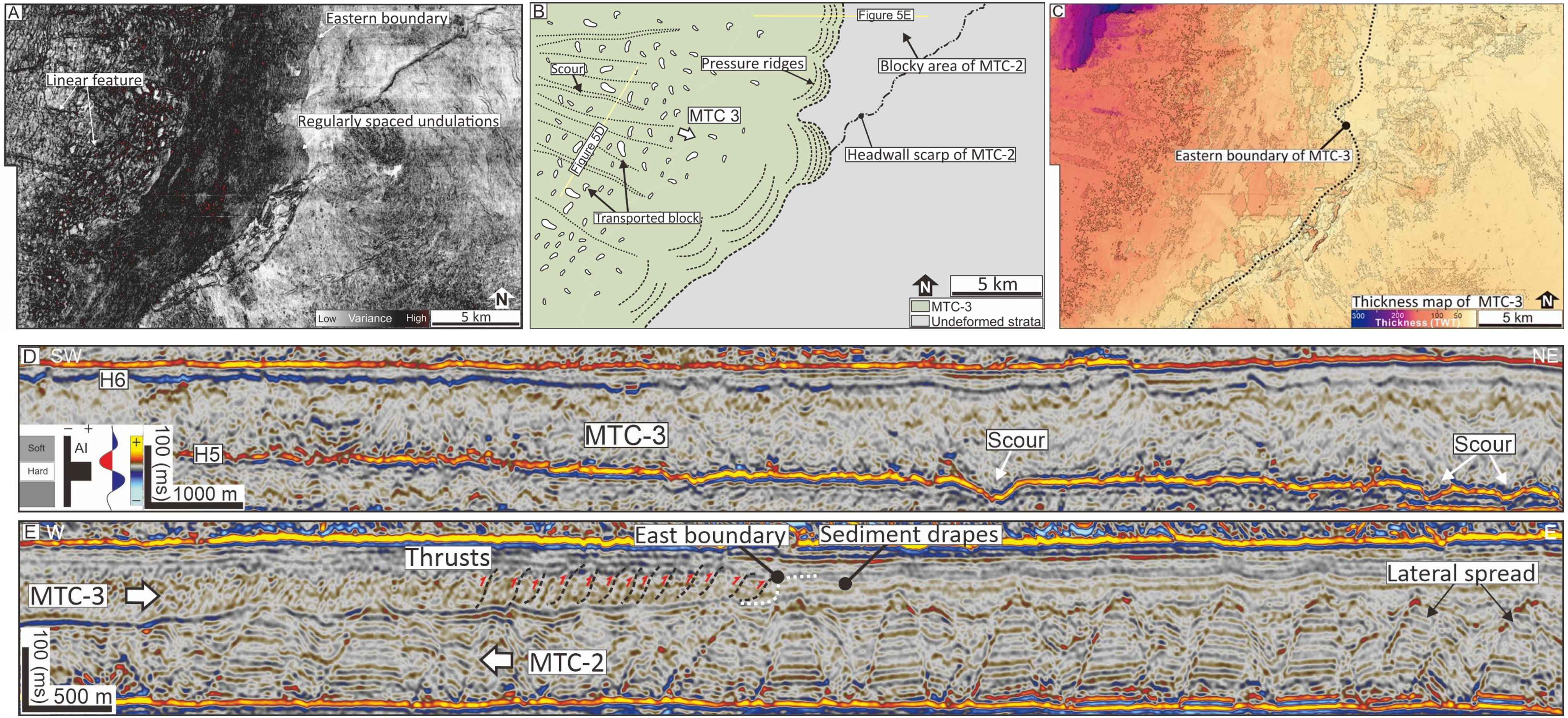

Figure 6: MTC-4

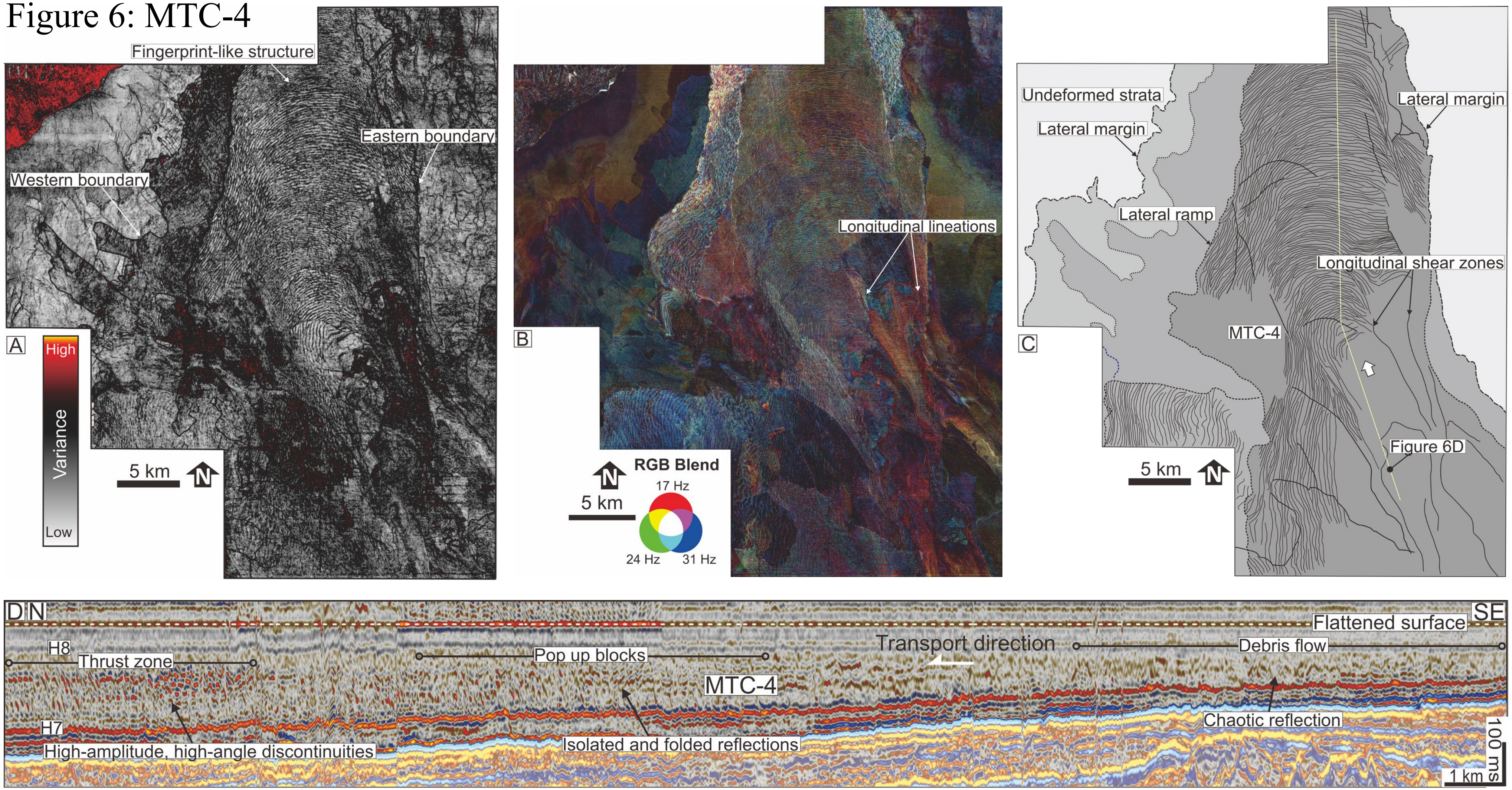

Figure 7_MTC-5

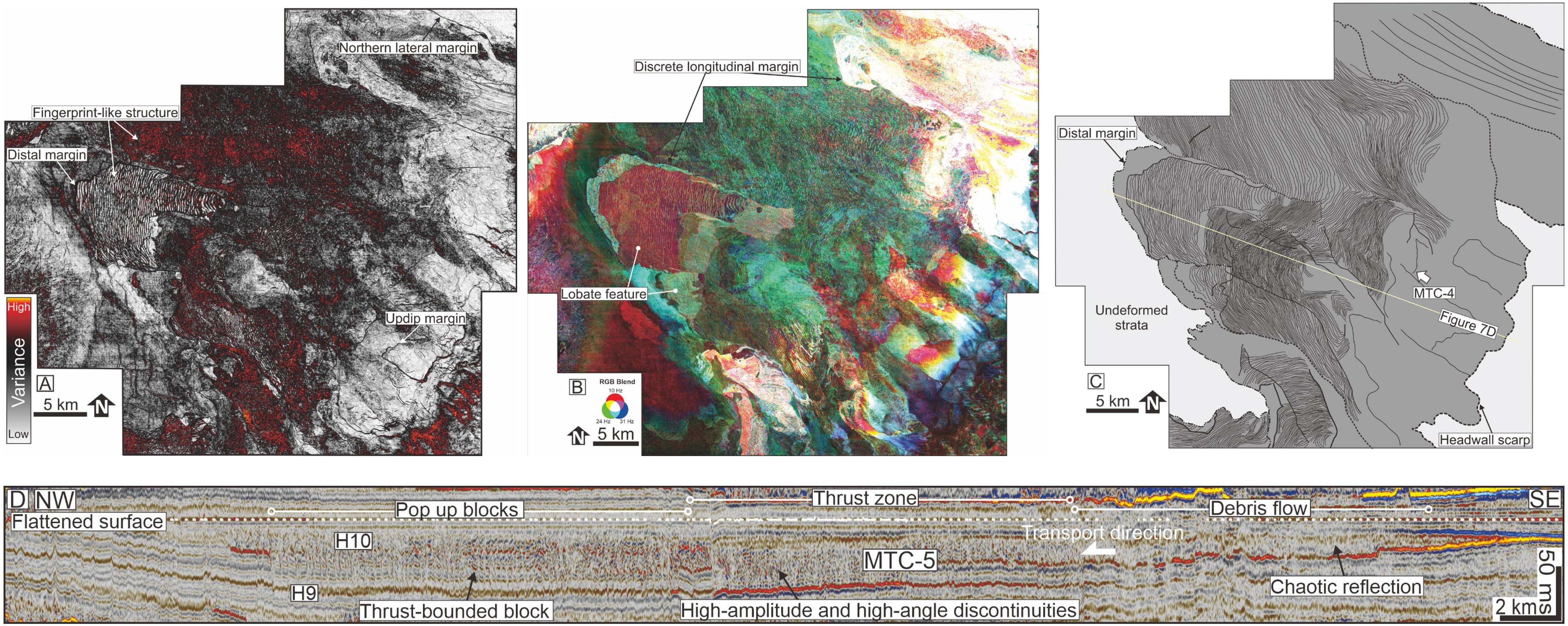

Figure 8_MTC-6&7

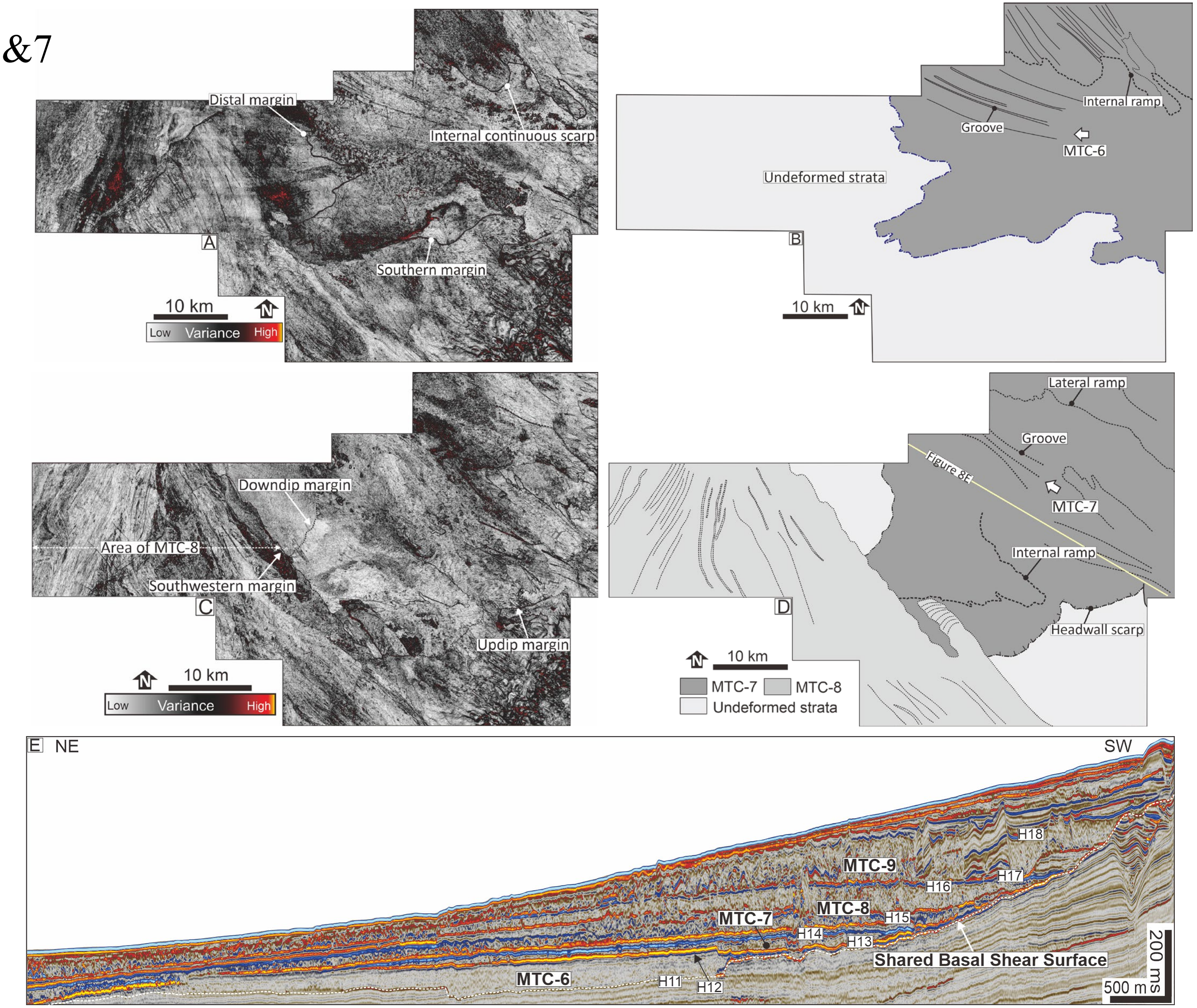

Figure 9_MTC-8

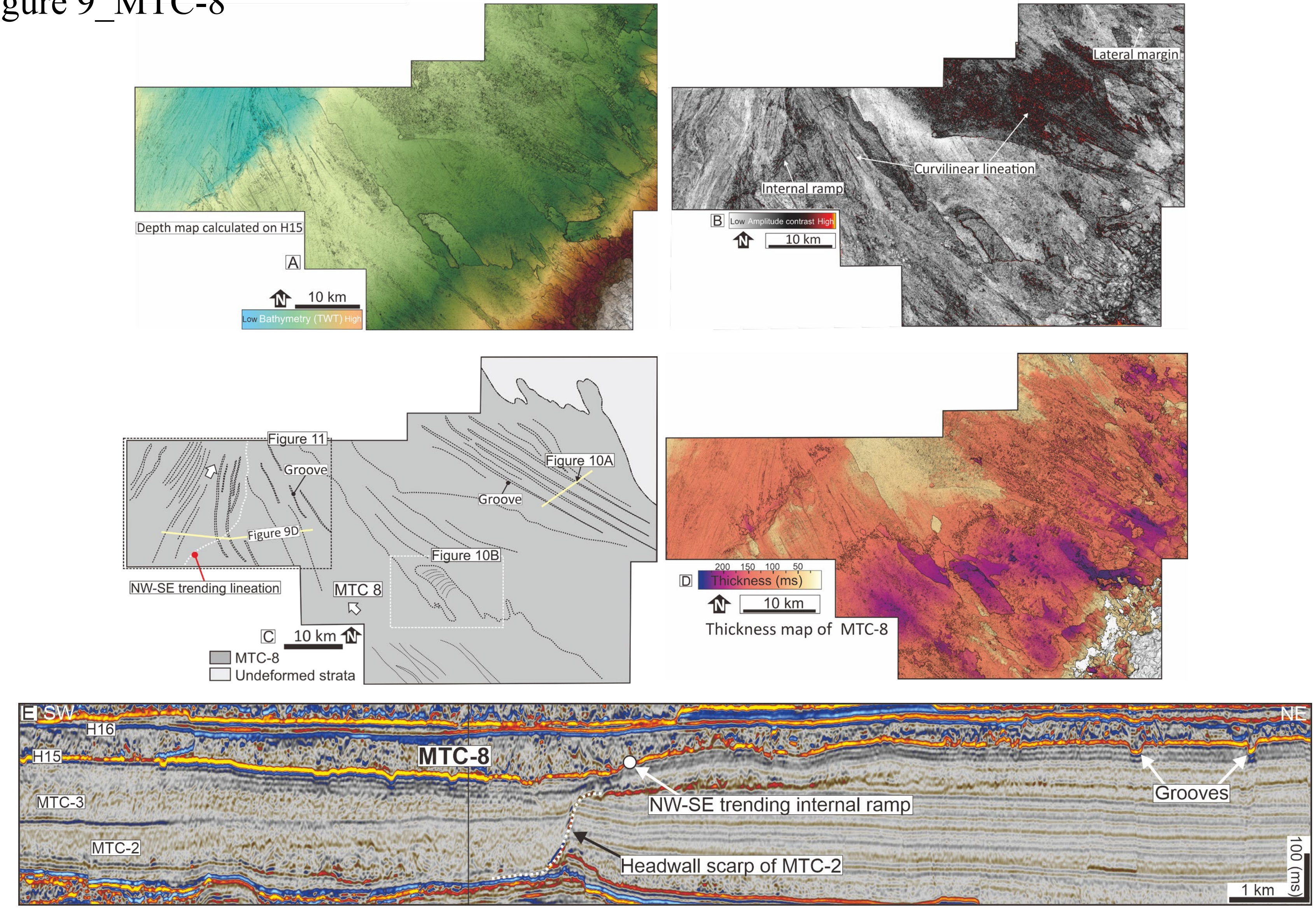

Figure 10_MTC-8

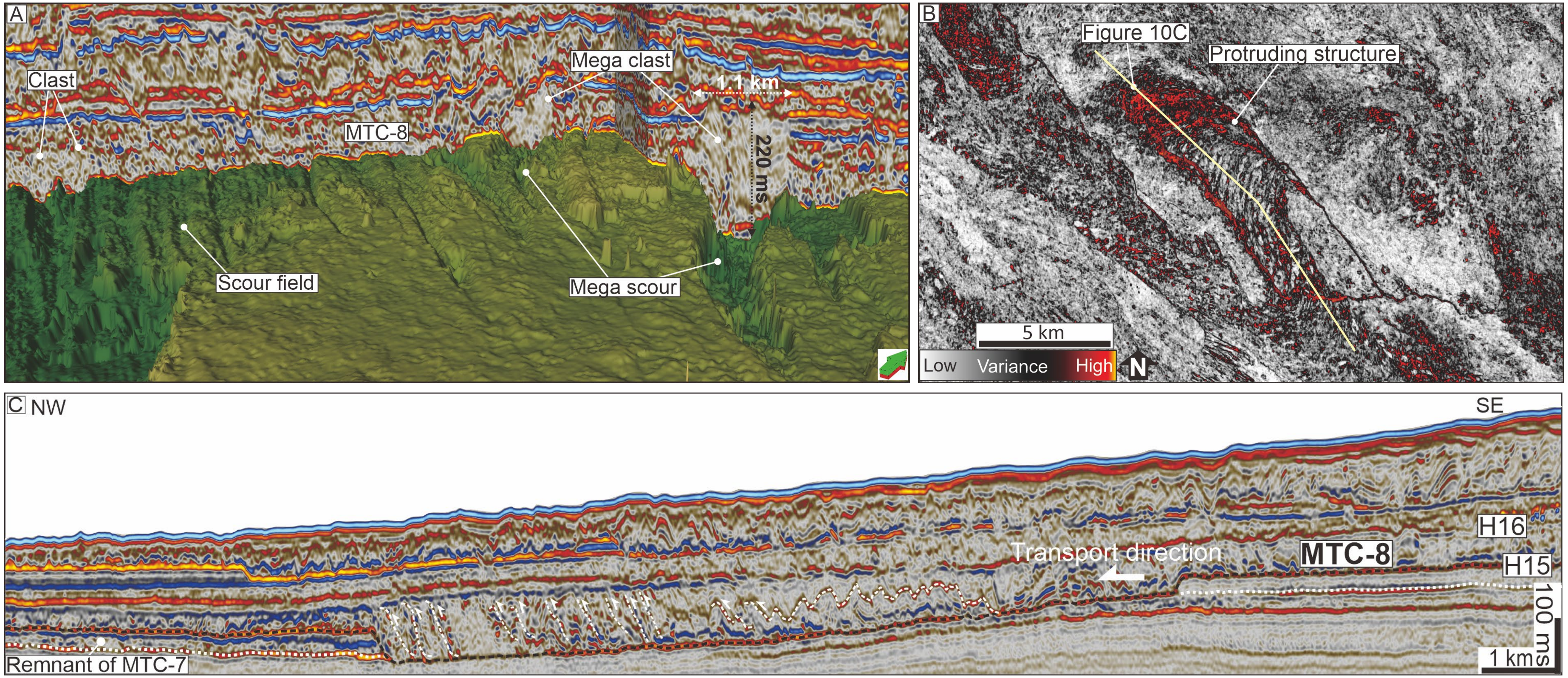

Figure 11_MTC-8

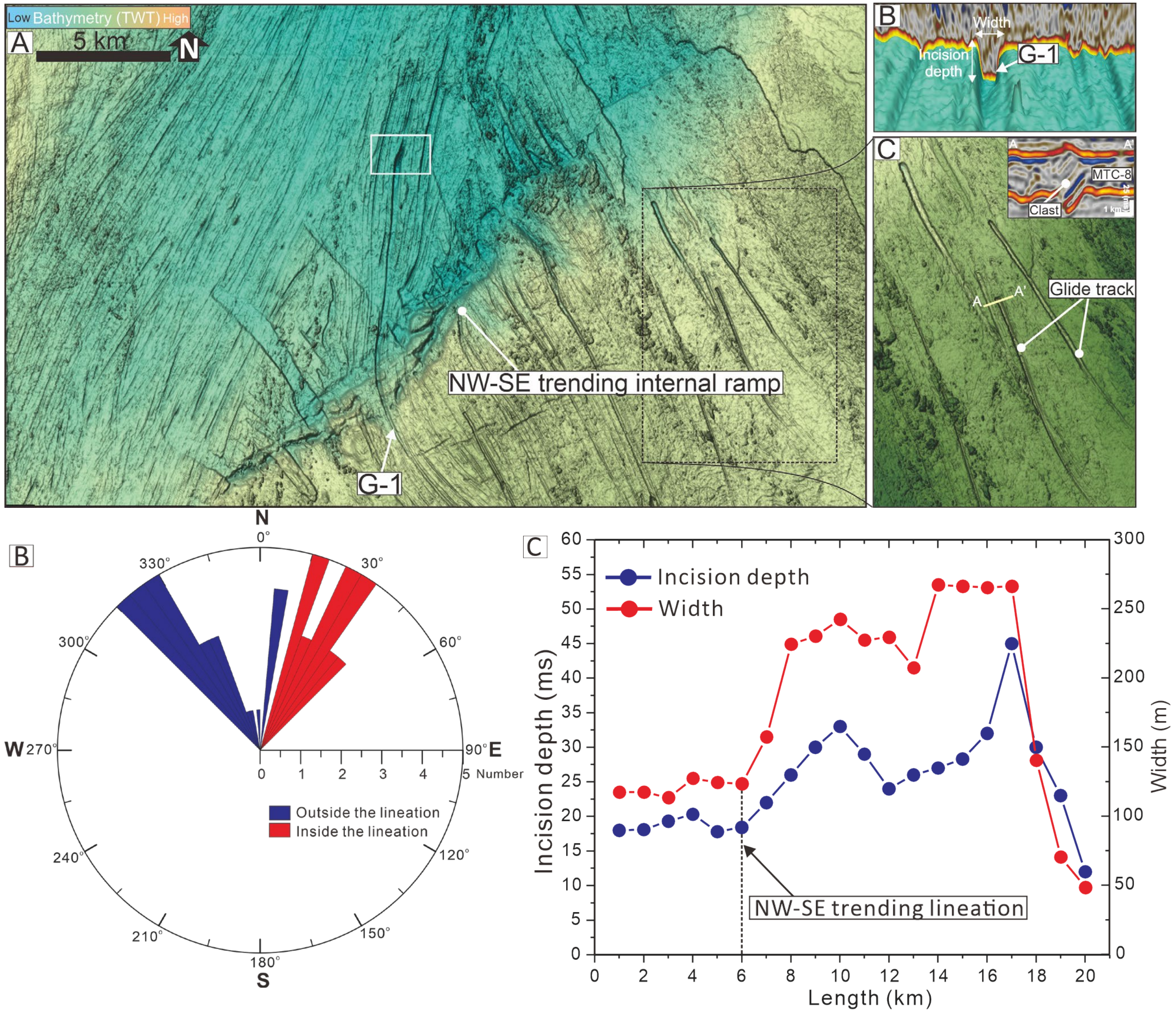

Figure 12_MTC-8; massive groove filed

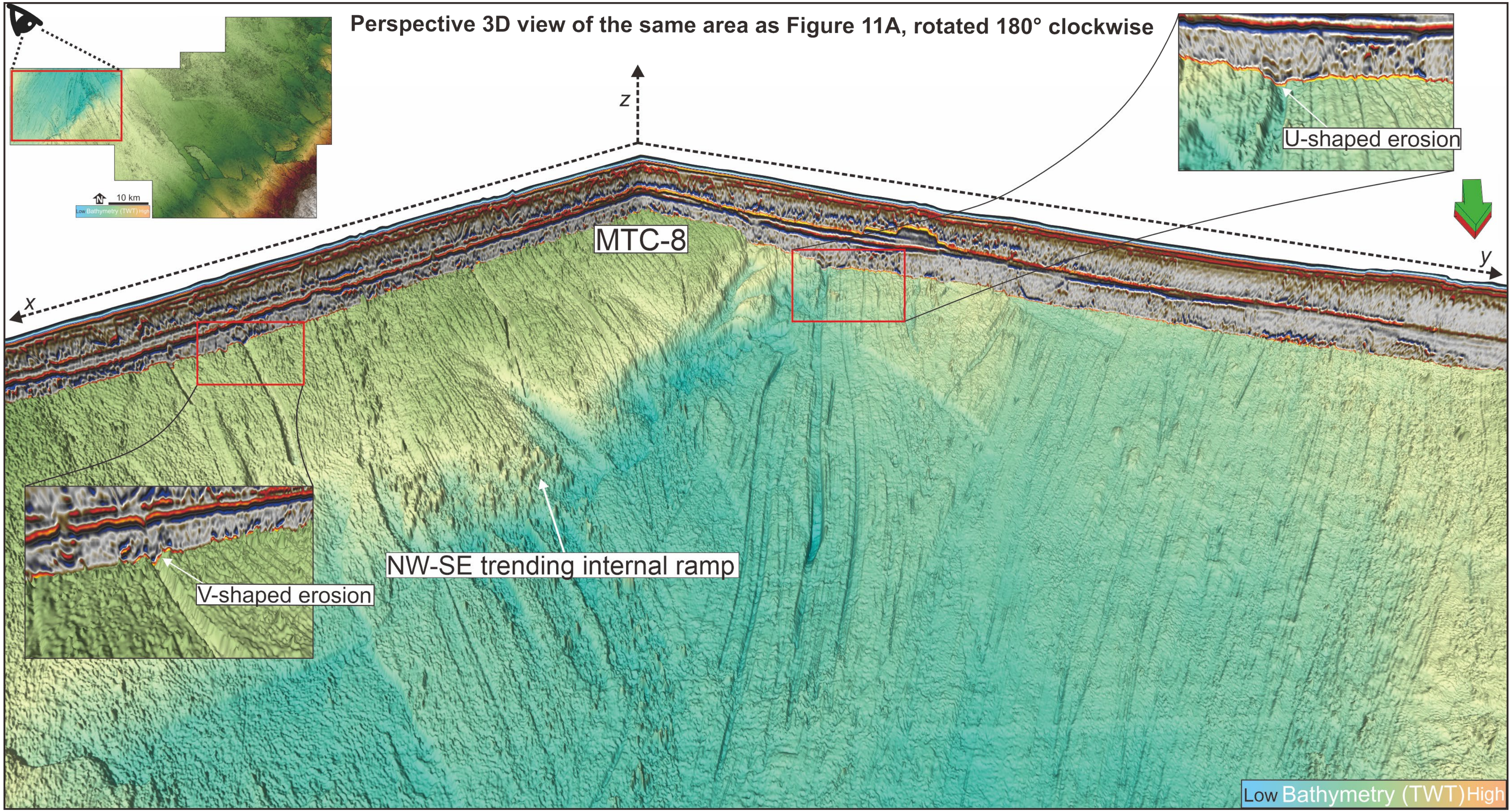

Figure 13_MTC-9

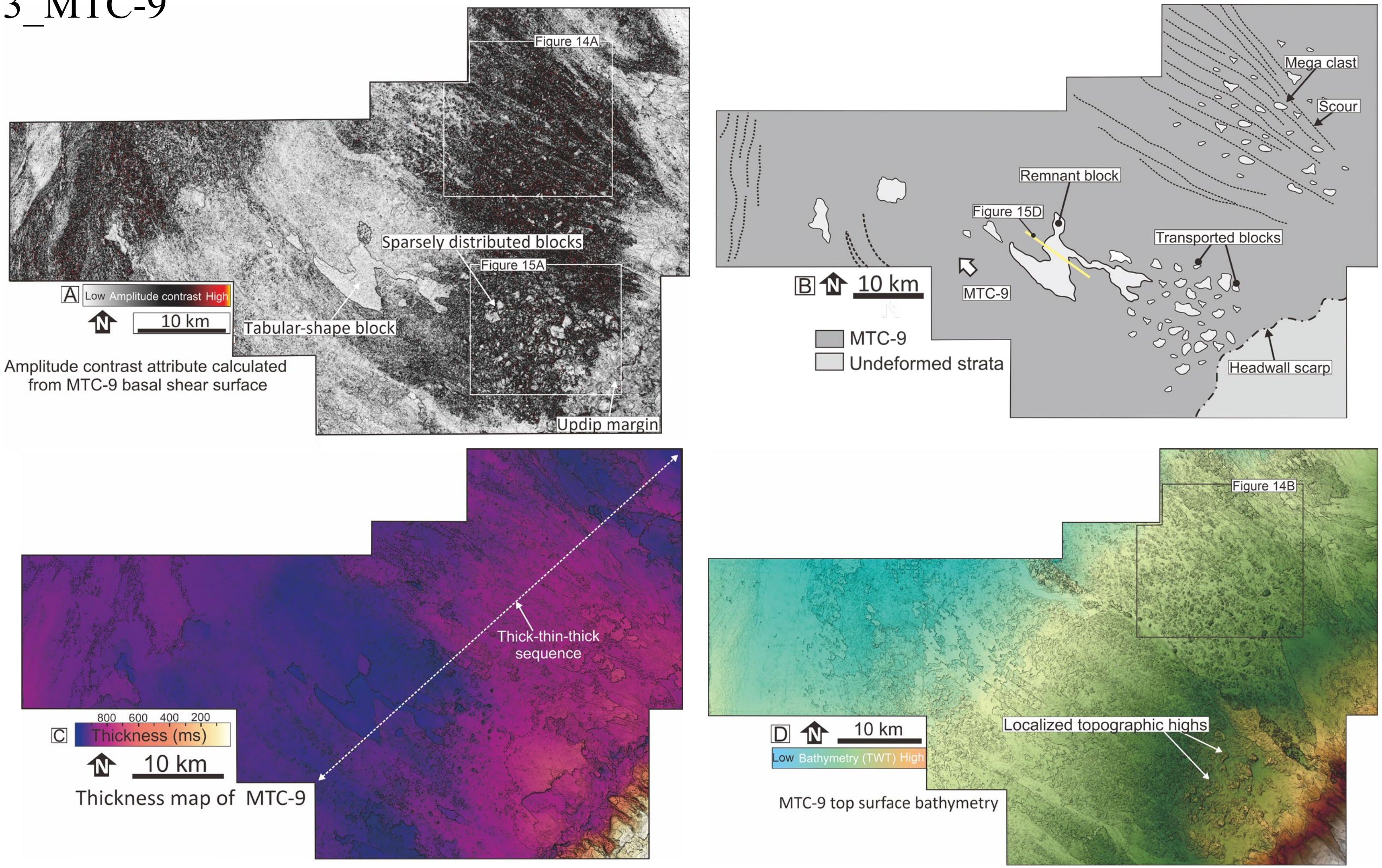

Amplitude contrast attribute calculated from MTC-9 basal shear surface

Thickness map of MTC-9

MTC-9 top surface bathymetry

Figure 14

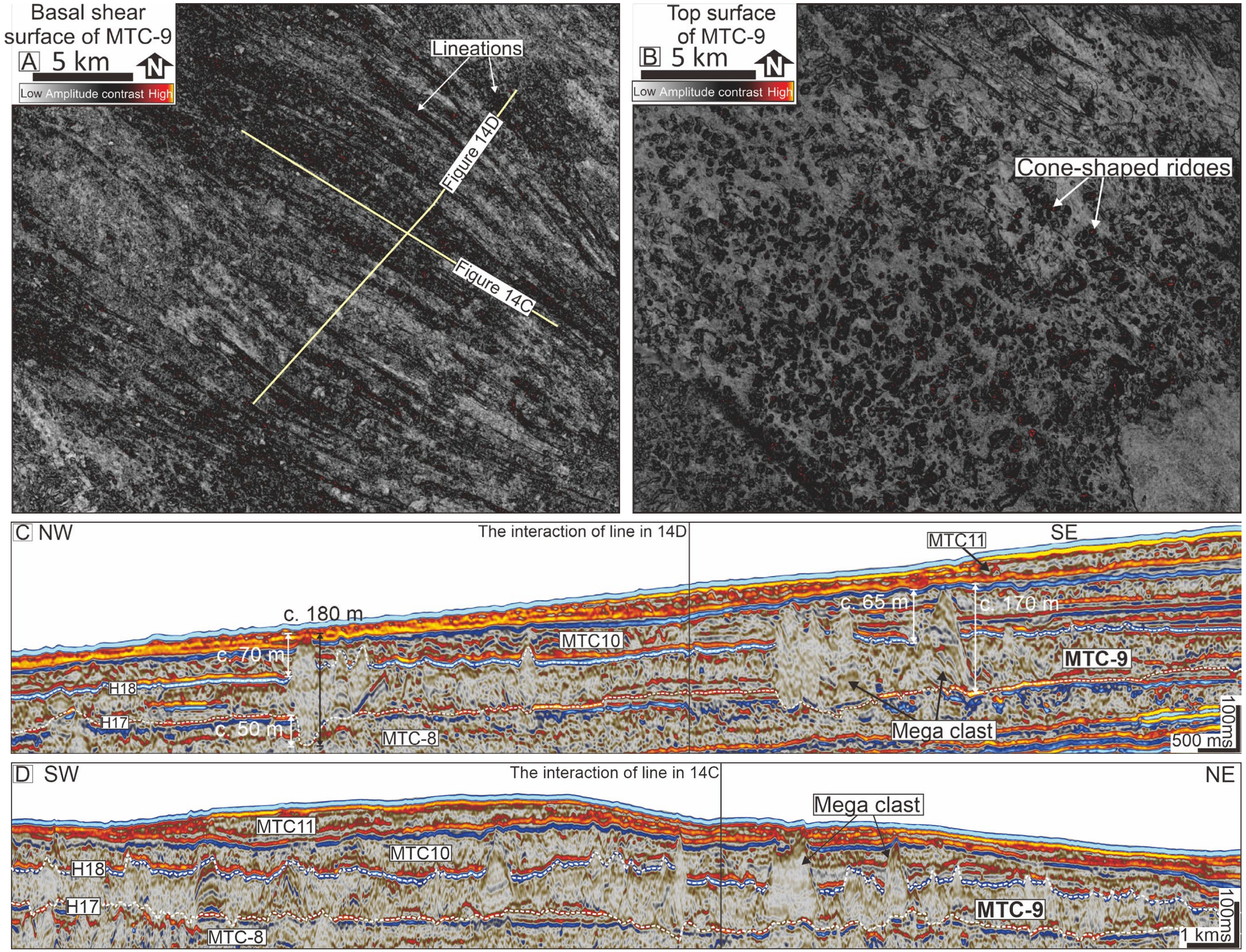
Basal shear surface of MTC-9
A
5 km
N
Low Amplitude contrast High
Lineations
Figure 14D
Figure 14C
Top surface of MTC-9
B
5 km
N
Low Amplitude contrast High
Cone-shaped ridges
C NW
The interaction of line in 14D
SE
MTC11
c. 180 m
c. 70 m
MTC10
H18
H17
c. 50 m
MTC-8
c. 65 m
c. 170 m
MTC-9
Mega clast
100ms
500 ms
D SW
The interaction of line in 14C
NE
Mega clast
MTC11
MTC10
H18
H17
MTC-8
MTC-9
100ms
1 kms

Figure 15_MTC-9 Blocks

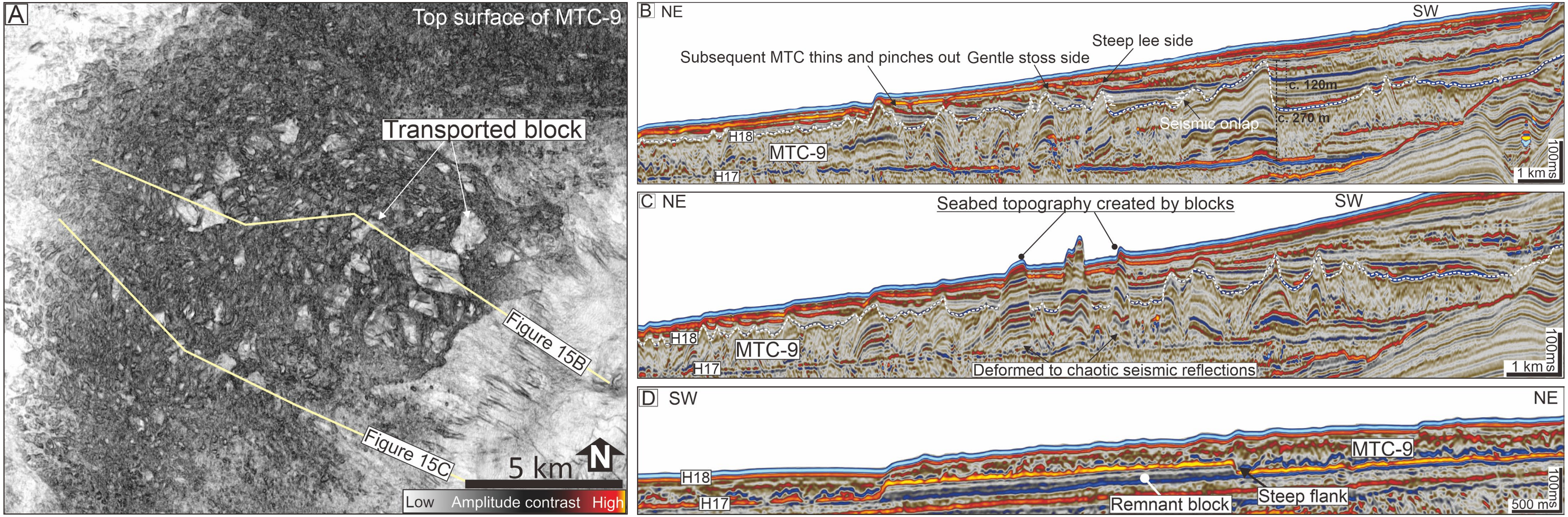

Figure 16; MTC-10&11

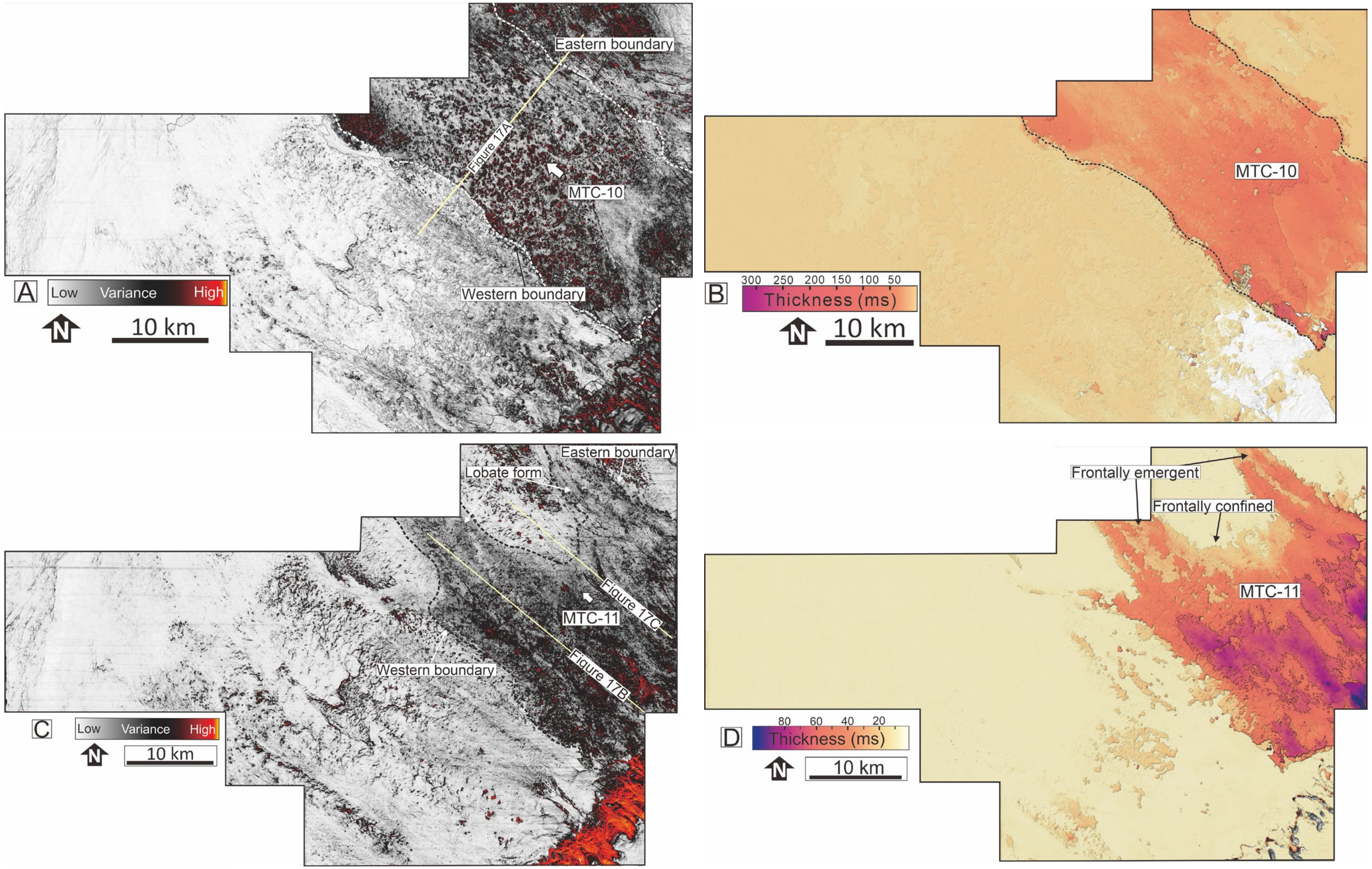

Figure 17

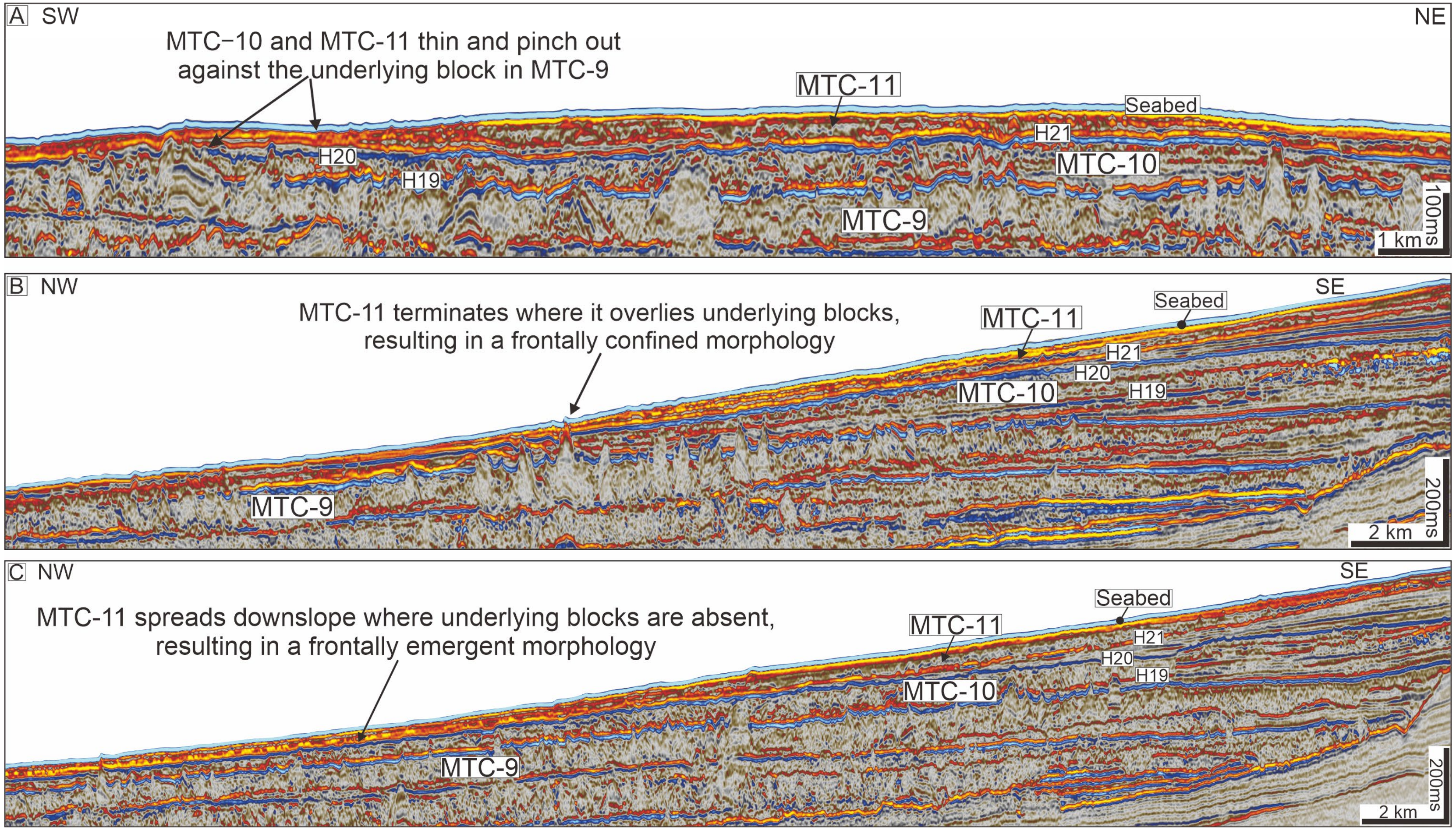
A
SW
NE
MTC–10 and MTC-11 thin and pinch out against the underlying block in MTC-9
MTC-11
Seabed
H21
H20
H19
MTC-10
MTC-9
100ms
1 km
B
NW
SE
MTC-11 terminates where it overlies underlying blocks, resulting in a frontally confined morphology
MTC-11
Seabed
H21
H20
H19
MTC-10
MTC-9
200ms
2 km
C
NW
SE
MTC-11 spreads downslope where underlying blocks are absent, resulting in a frontally emergent morphology
Seabed
MTC-11
H21
H20
H19
MTC-10
MTC-9
200ms
2 km

Figure 18

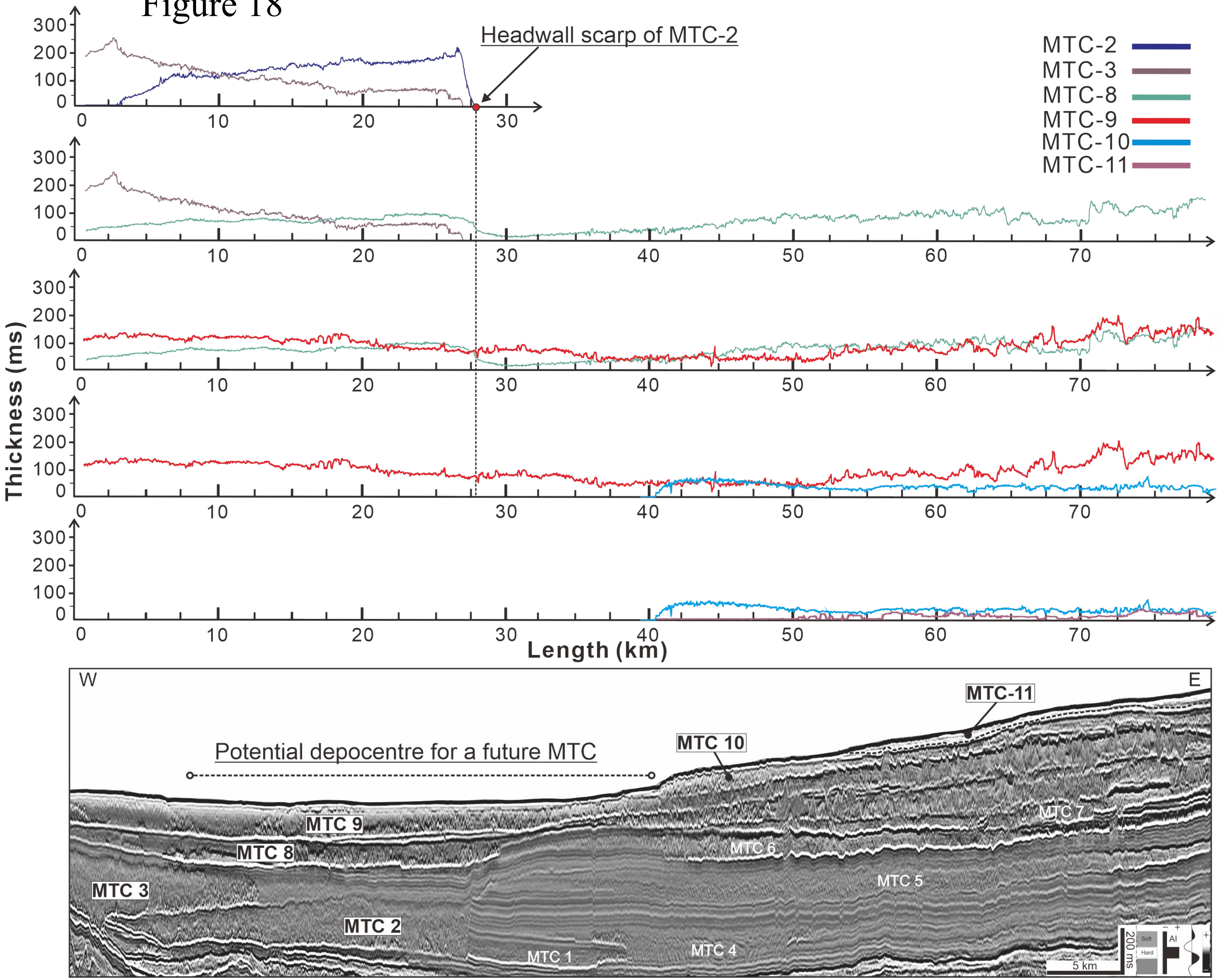
Headwall scarp of MTC-2
MTC-2
MTC-3
MTC-8
MTC-9
MTC-10
MTC-11
Thickness (ms)
300
200
100
0
0
10
20
30
40
50
60
70
Length (km)
W
E
Potential depocentre for a future MTC
MTC 10
MTC-11
MTC 9
MTC 8
MTC 3
MTC 2
MTC 1
MTC 4
MTC 5
MTC 6
MTC 7
5 km
200 ms
Soft
Hard
AI
+
-

Figure 19

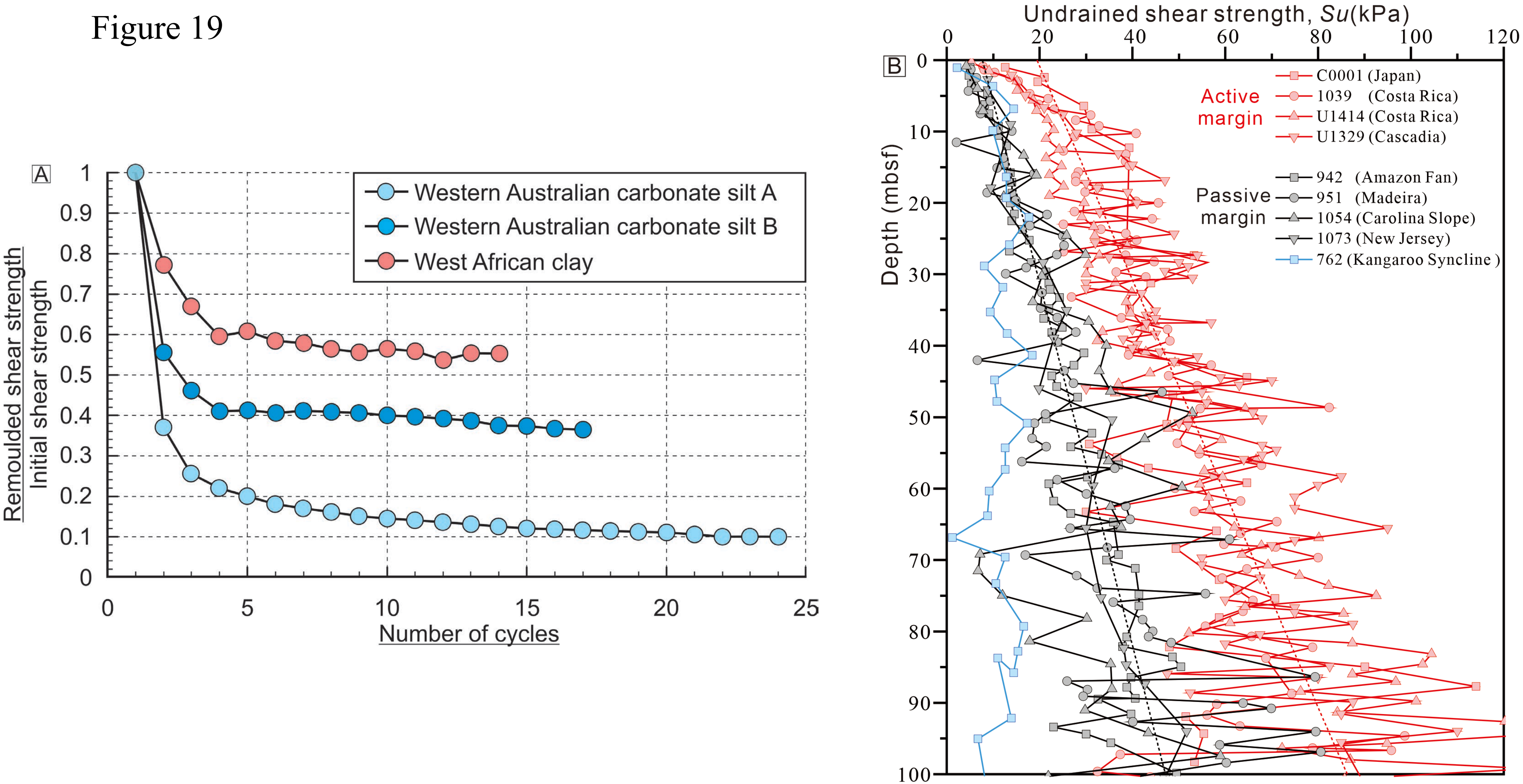
A
Remoulded shear strength
Initial shear strength
1
0.9
0.8
0.7
0.6
0.5
0.4
0.3
0.2
0.1
0
0
5
10
15
20
25
Number of cycles
Western Australian carbonate silt A
Western Australian carbonate silt B
West African clay
B
Undrained shear strength, Su(kPa)
0
20
40
60
80
100
120
Depth (mbsf)
0
10
20
30
40
50
60
70
80
90
100
Active margin
C0001 (Japan)
1039 (Costa Rica)
U1414 (Costa Rica)
U1329 (Cascadia)
Passive margin
942 (Amazon Fan)
951 (Madeira)
1054 (Carolina Slope)
1073 (New Jersey)
762 (Kangaroo Syncline)